



ISC – Impatti sul Suolo e sulle Coste

**Numerical analyses of rainfall-
induced landslides.
The case of Nocera Inferiore, March
2005**

prof. Luciano Picarelli

Analisi e Monitoraggio del Rischio Ambientale, AMRA

prof. Filippo Vinale

Analisi e Monitoraggio del Rischio Ambientale, AMRA



Numerical analyses of rainfall-induced landslides. The case of Nocera Inferiore, March 2005

Summary

The following report contains the results of 2D numerical simulations intended to reproduce the rain induced seepage process which triggered the Nocera landslide of March 4, 2005. Particular attention has been dedicated to focus on the effects of rainfall on pore water pressure distribution and flow rate over the slope domain and on the slope stability progress over time.

Keywords: rainfall-induced landslide, slope stability analysis, numerical simulation

JEL Classification:

Address for correspondence:

prof. Luciano Picarelli
E-mail: luciano.picarelli@amracenter.com

A.M.R.A. S.c.a.r.l.
Via Nuova Agnano, 11
80125 Napoli, Italy



CONTENTS

1. Introduction.....	4
2. The model adopted in the analyses.....	6
2.1 Initial and boundary conditions.....	6
2.2 Soil Parameters.....	6
2.3 Pore water pressures and flow rates in the hypothesis of free draining slope bottom	7
2.4 Pore water pressures and flow rates in the hypothesis of impervious slope bottom.....	14
2.5 Safety factors.....	21
3. Rain induced effects for rain forecasts.....	22



1. Introduction

The following report illustrates numerical results obtained from simulating the rain induced seepage process which triggered the Nocera landslide of March 4, 2005.

Figure 1 plots daily rainfall measured during the time period of 7 months which preceded the mentioned flowslide. The same figure represents the evolution of cumulative rainfall from August 1, 2004 up to the day of the flowslide. Two exceptional rainfall events occurred in the time period considered. During the first, occurring on December 26, 2004, 164 mm of rain fell in 24 hours (460 mm had fallen in the previous two months). This event was not associated to any flowslide. The second significant rainfall produced the flowslide around two months later at a similar level (161 mm) of rainfall cumulative in the previous 24 hours (531 mm had fallen in the previous two months). After the main flowslide trigger, 24-hour cumulative rainfall rose to around 200 mm and flowslides in the area kept on triggering.

In order to take into account the effects of precipitations the rainfall in the last six months prior to the landslide triggering were analyzed.

The problem was analyzed by assuming a plane flow in the assumption of rigid soil skeleton. 2D analyses were carried out by the use of the finite element program SEEP/W code (produced by the GEO-SLOPE International Ltd), which has allowed to solve the Richards' equation taking into account the slope geometry plotted in Figure 2. The real geometry was simplified in order to make isolate the role of the boundary conditions.

In particular, this report focuses on the effects of rainfall on:

- pore water pressure distribution over the slope domain
- flow rate vectors over the slope domain
- global safety factor of the slope over time.

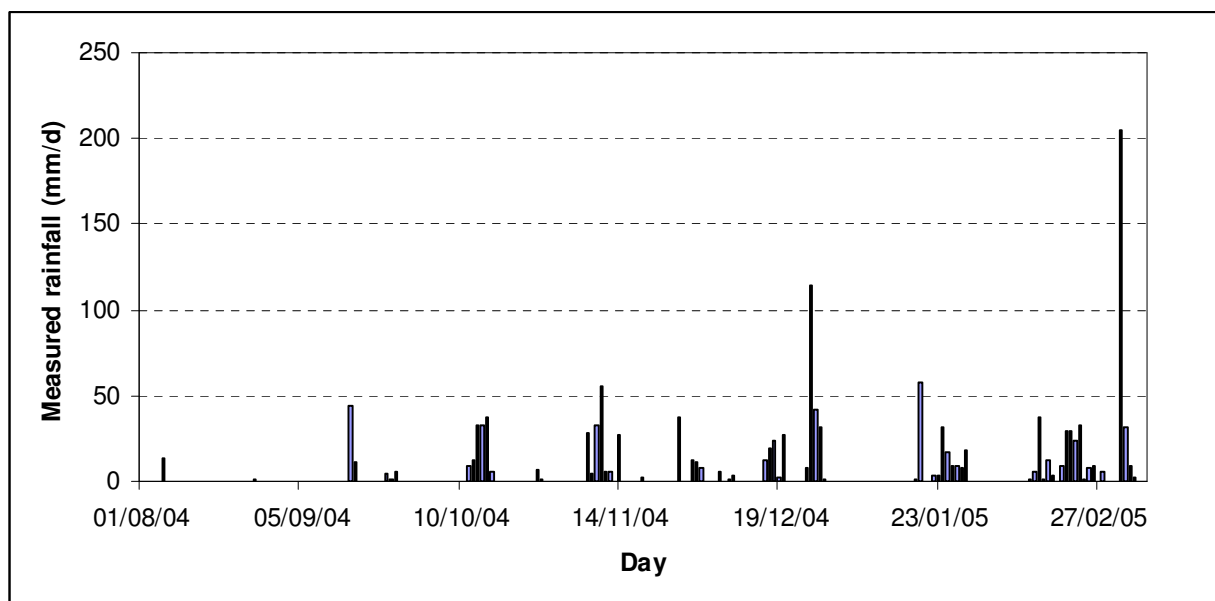


Figure 1. Daily rains from August 2004 up to the triggering time (March 4, 2005)

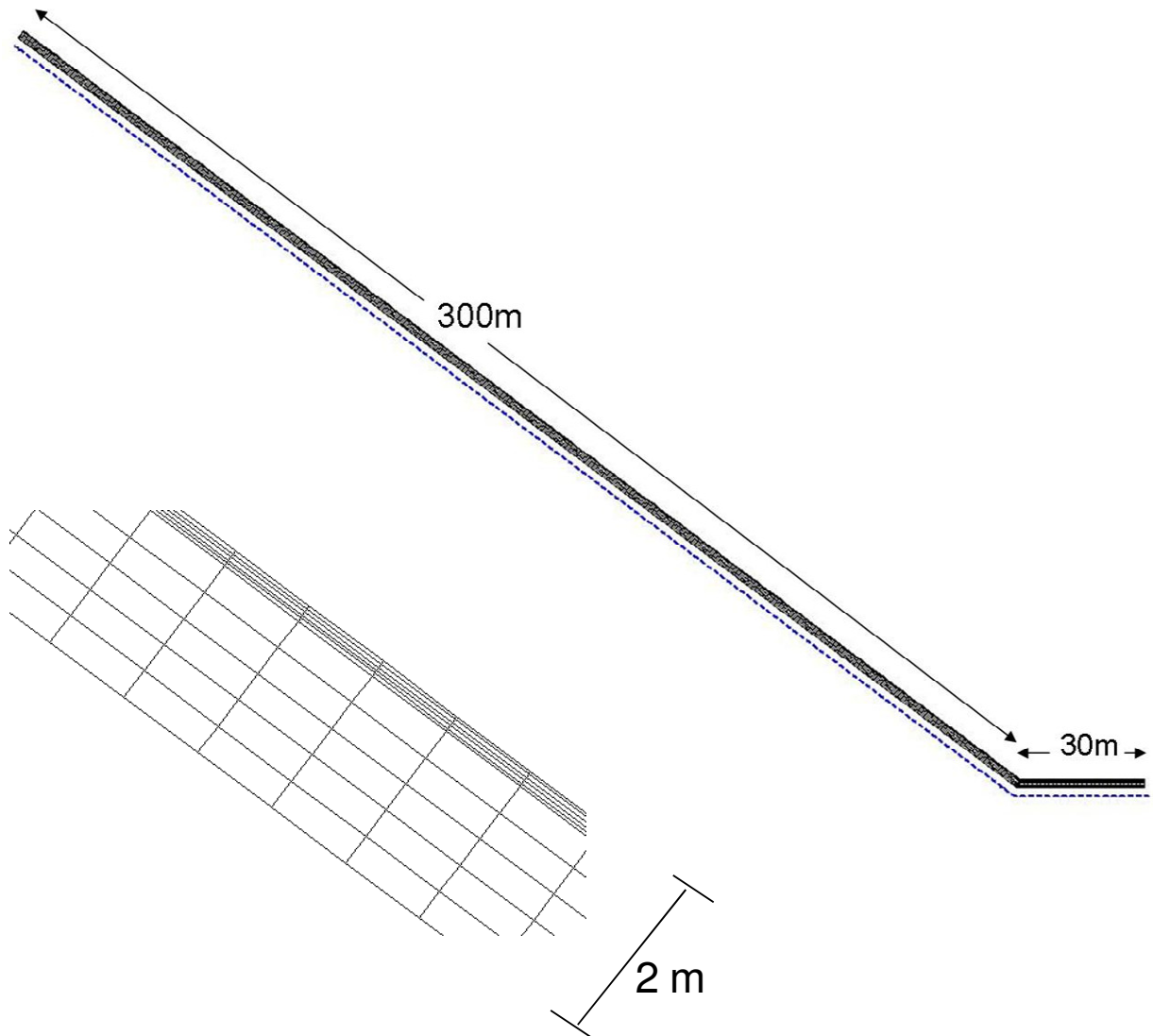


Figure 2. The finite element mesh



2. The model adopted in the analyses

The phenomenon is regulated by the subsequent law, valid inside the domain:

$$\frac{\partial}{\partial y} \left(k_y \frac{\partial H}{\partial y} \right) + Q = \frac{\partial \eta}{\partial t}$$

- Q applied boundary flux;
- k_y hydraulic conductivity in the y – direction;
- H total head;
- η volumetric water content;

2.1 Initial and boundary conditions

At the upper boundary of the analyzed domain a hydraulic condition regulated by the rainfall history is applied. A transient calculation is then performed. Flow rate normal to the boundary was assumed equal to the projected rainfall intensity, up to boundary pore water pressure not exceeding atmospheric pressure. For higher pore pressure values, pore water pressure is set at atmospheric pressure. While the latter condition is forced, flow rate is controlled so as not to exceed the normally projected rainfall intensity.

Initial conditions were defined for each vertical as a linear change of suction with depth characterized by a gradient equal to the water specific weight. Initial suction is equal to about 20 kPa at the slope base and to about 50 kPa at the slope surface. This distribution was forced by assigning a hydrostatic condition consistent with a fictitious water table placed below the slope base. In this way, initial suction even represent at each point the values suction tends to during dry periods.

Two boundary conditions at the base of the slope were considered: impervious and free draining bottom.

As described in a previous report, the calcareous bedrock is highly fractured, providing therefore in principle the possibility for the pore water to drain freely at the bottom surface of the pyroclastic cover. On the other hand, the downward seepage process developed in the past centuries through the pyroclastic cover may have in several cases moved downward the finest soil component, filling the calcareous fractures and reducing significantly the drainage potentiality of the bedrock. This latter condition may practically correspond to an impervious boundary condition.

2.2 Soil parameters



The water retention curve used in the model was obtained experimentally through oedometric laboratory tests carried out on samples of reconstituted pyroclastic soils. The permeability function was obtained from the saturated permeability of these materials (average of 10^{-6} cm/s), by extrapolating it to unsaturated conditions through the soil water retention curve. In order to validate the model in its ability to reproduce real developments of soil suction over time, a monitoring station was installed in the area where the landslides were triggered. Monitored soils are very similar to those constituting the shallow layer involved in the main landslide of March 2005. The monitoring station was equipped with instruments to measure atmospheric variables and soil suction (Jet-fill tensiometers) at different depths. As is well known, Jet-fill may measure soil suction up to 80 kPa. They may be reliably used in such types of soils since suction values typically do not exceed 70 kPa. Soils parameters were adjusted up to make predicted suction values consistent with measured ones during a time period of 2 months. Prediction were obviously carried out by imposing hydraulic boundary conditions derived from the monitored rain.

2.3 Pore water pressures and flow rates in the hypothesis of free draining slope bottom

The free draining boundary condition at the bottom of the pyroclastic layer has been modeled by assuming that the water flow rate be governed by the permeability coefficient of the soil under a unit gradient. In this way, since the soil permeability is assumed to increase with increasing the degree of saturation (i.e., the gravity is assumed to act alone in driving water out of the system from the bottom of the slope domain) the flow rate itself increases during wet periods and decreases during dry periods.

The free draining boundary condition has been assumed only at the bottom of the sloping part of the geometrical domain. At the bottom of the horizontal part an impervious condition has been assumed instead. The upstream and downstream vertical boundaries have been finally modeled as a seepage surfaces.

Figures from 3 to 14 plot the pore water pressure contours and the flow rate vectors at different times of the real rain history.

In general, the evolution of contours indicates a progressive and extensive increase in pore water pressure (i.e., a decrease in suction). Pore water pressures cumulates over time indicating that there is a significant and increasing influence of rains fallen during the last months.

In the uppermost part (see Figures 3-6-9-12) the range of suction on 2004, 1st December was in between 14-38 kPa. It decreased subsequently down to attain 12-24kPa on 2005, 1st February, 10-22kPa on the day before the landslide trigger (2005, 3rd February) and 3-9kPa on the landslide day, 2005, 4th February at 16.00 o' clock. Therefore in the free draining hypothesis at the bottom surface, at the flowslide time suction is showed to be very close to zero.

In the middle part (Figures 4-7-10-13) and in the lowermost part (Figures 5-8-11-14) of the geometrical scheme suction levels are almost the same as in the uppermost part



for the same times considered above. Only in a small zone of the lowermost part, positive pore water pressure values take place (Figure 14)

Flow rate vectors indicate that the water flow is directed vertically and downward over the entire time period analyzed. As expected, the flow follows approximately a one dimensional pattern due to the hypothesis of free draining boundary, that is, the hydraulic behavior might be predicted by referring to simpler and less cumbersome one dimensional analyses.

However, in the lowermost part of the slope two effects make the water flow a little bit more complex. In fact, the water does not flow vertically due to two factors which make the problem a real two dimensional problem. A first factor is the potentiality for top horizontal surface to collect a volume of rain water higher than that for the sloped part. This produces higher pore water pressures within the downstream domain and, as a consequence, flow vectors which are directed upstream. The same effect (pore water pressure higher downstream and flow vectors directed upstream) is enhanced by the presence of the impervious boundary at the bottom of the horizontal part.

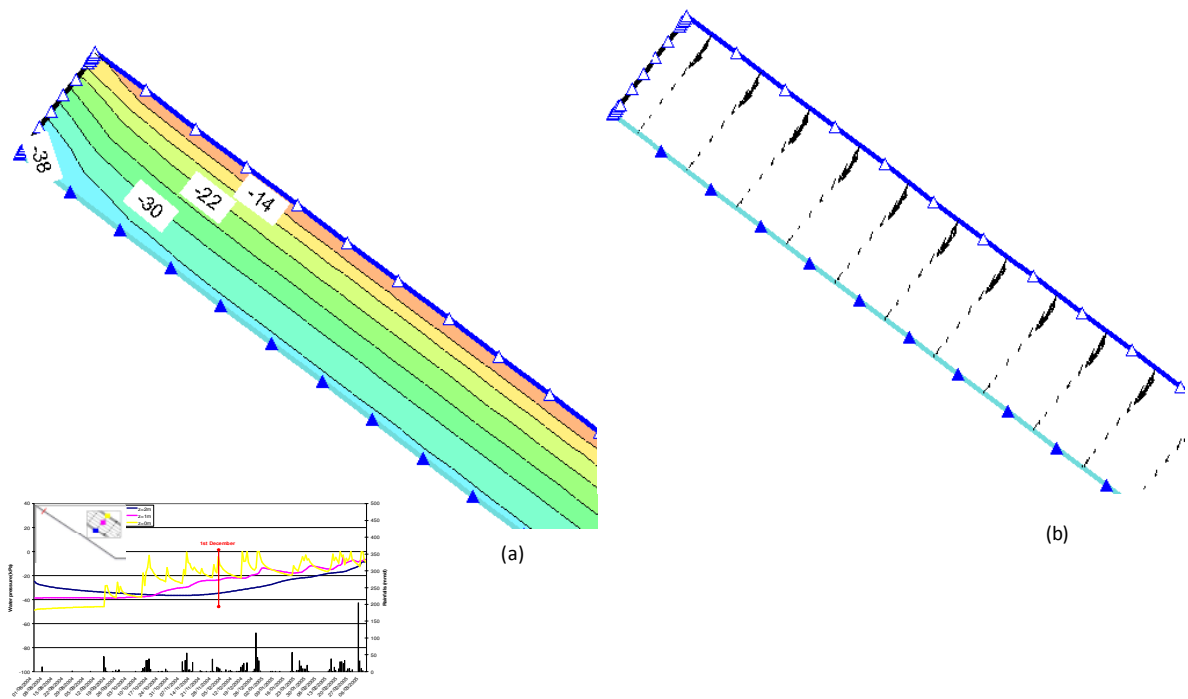


Figure 3. Pore pressure contours (a) and flow rate vectors (b) predicted on December 1 within the upper zone of the geometrical scheme, by assuming unit gradient at the base of the scheme and seepage flow at lateral boundaries

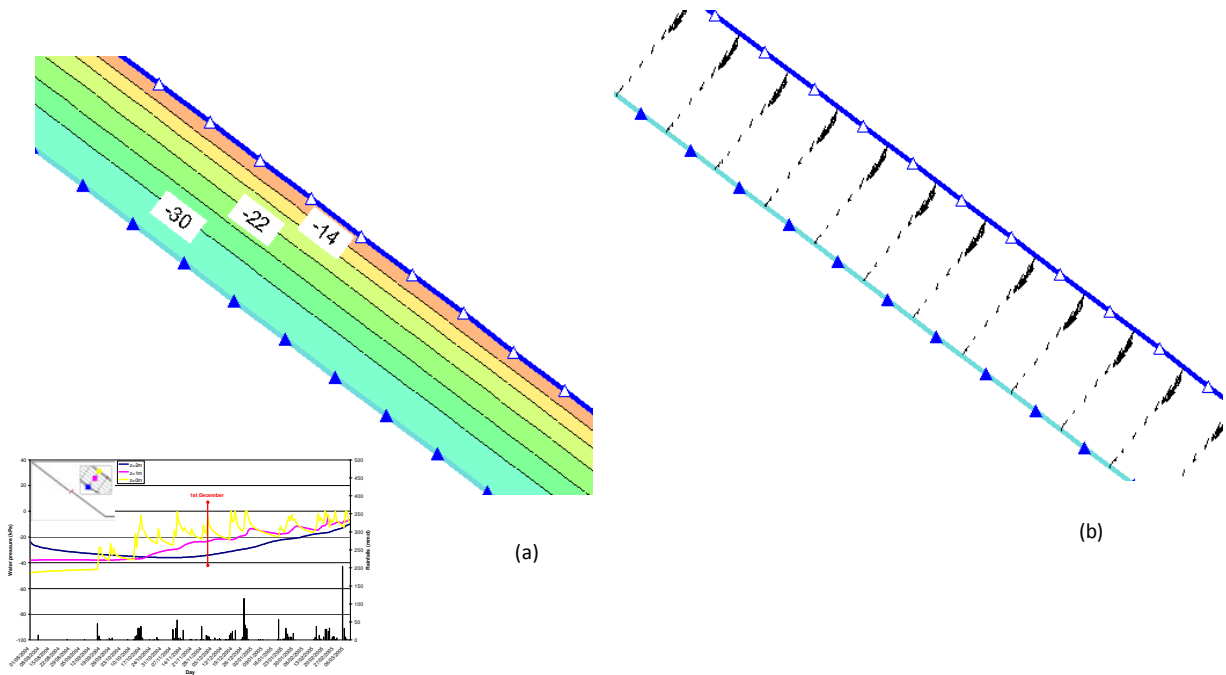


Figure 4. Pore pressure contours (a) and flow rate vectors (b) predicted on December 1 within the central zone of the geometrical scheme, by assuming unit gradient at the base of the scheme and seepage flow at lateral boundaries

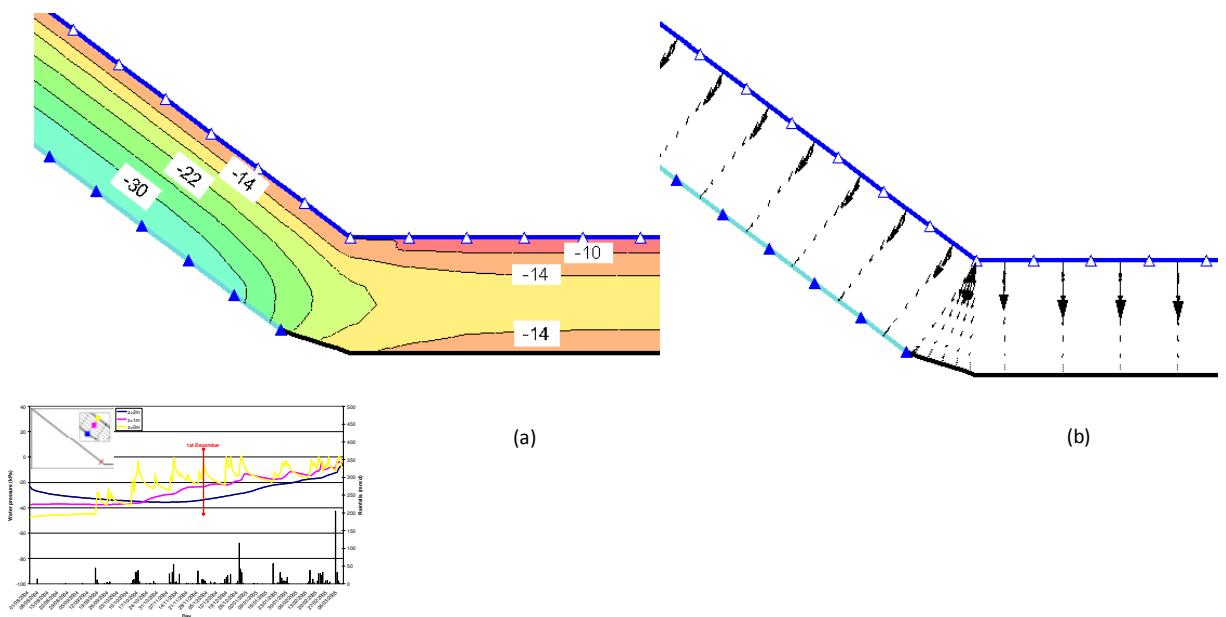


Figure 5. Pore pressure contours (a) and flow rate vectors (b) predicted on December 1 within the lower zone of the geometrical scheme, by assuming unit gradient at the base of the scheme and seepage flow at lateral boundaries

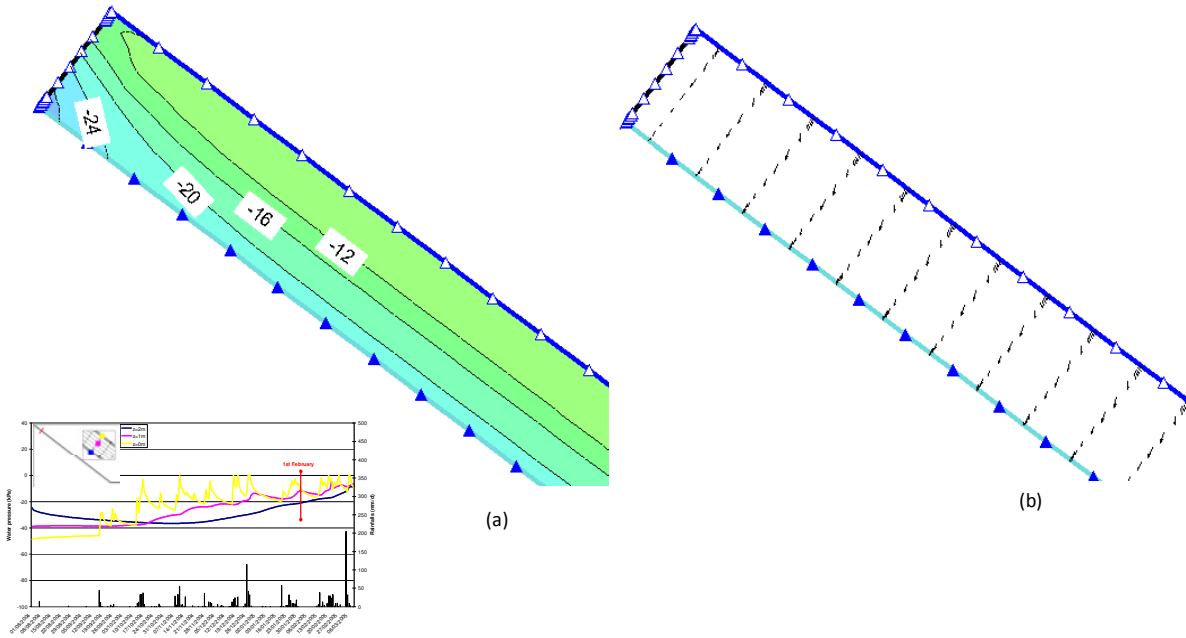


Figure 6. Pore pressure contours (a) and flow rate vectors (b) predicted on February 1 within the upper zone of the geometrical scheme, by assuming unit gradient at the base of the scheme and seepage flow at lateral boundaries

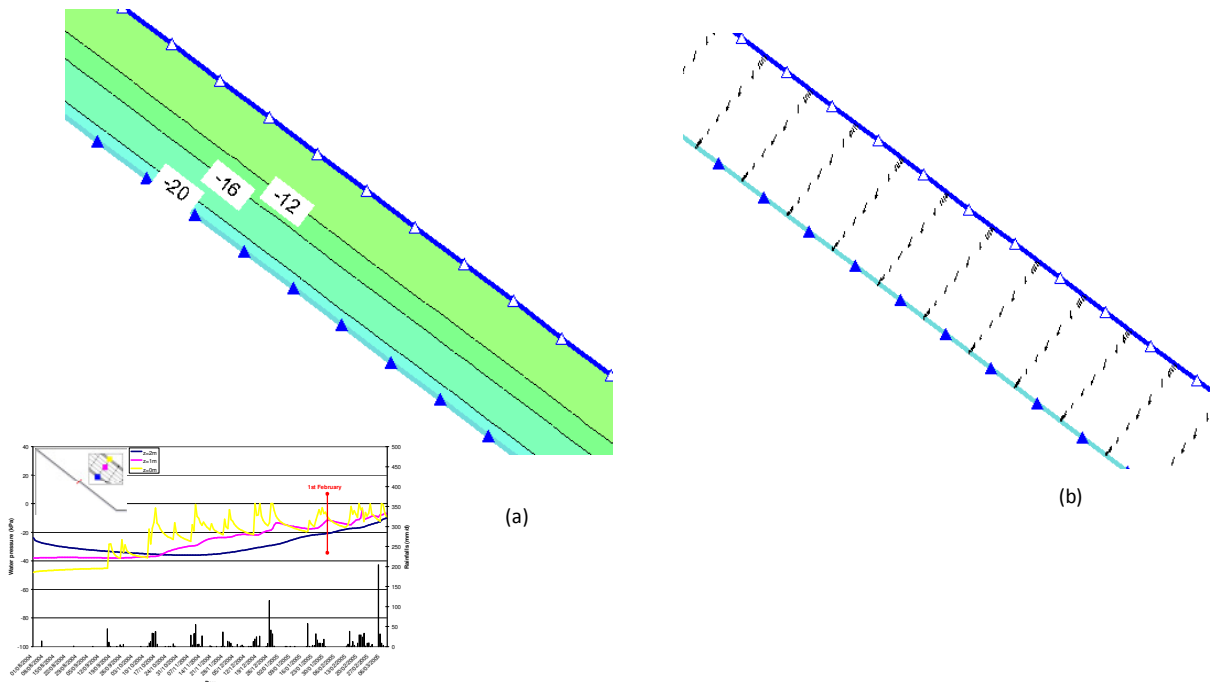


Figure 7. Pore pressure contours (a) and flow rate vectors (b) predicted on February 1 within the central zone of the geometrical scheme, by assuming unit gradient at the base of the scheme and seepage flow at lateral boundaries

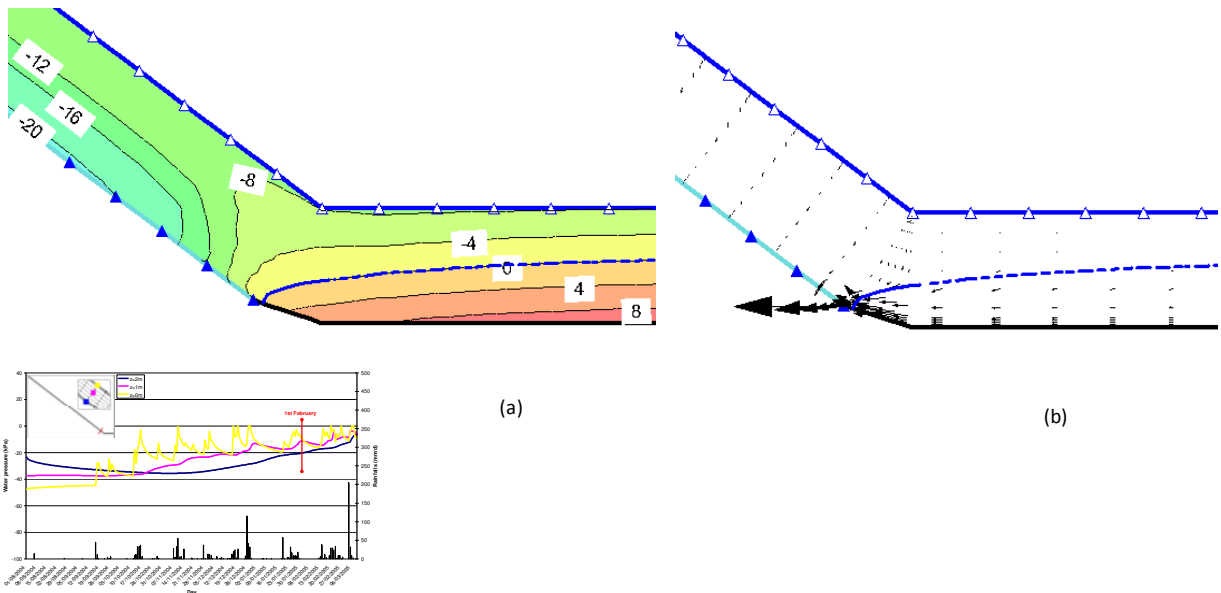


Figure 8. Pore pressure contours (a) and flow rate vectors (b) predicted on February 1 within the lower zone of the geometrical scheme, by assuming unit gradient at the base of the scheme and seepage flow at lateral boundaries

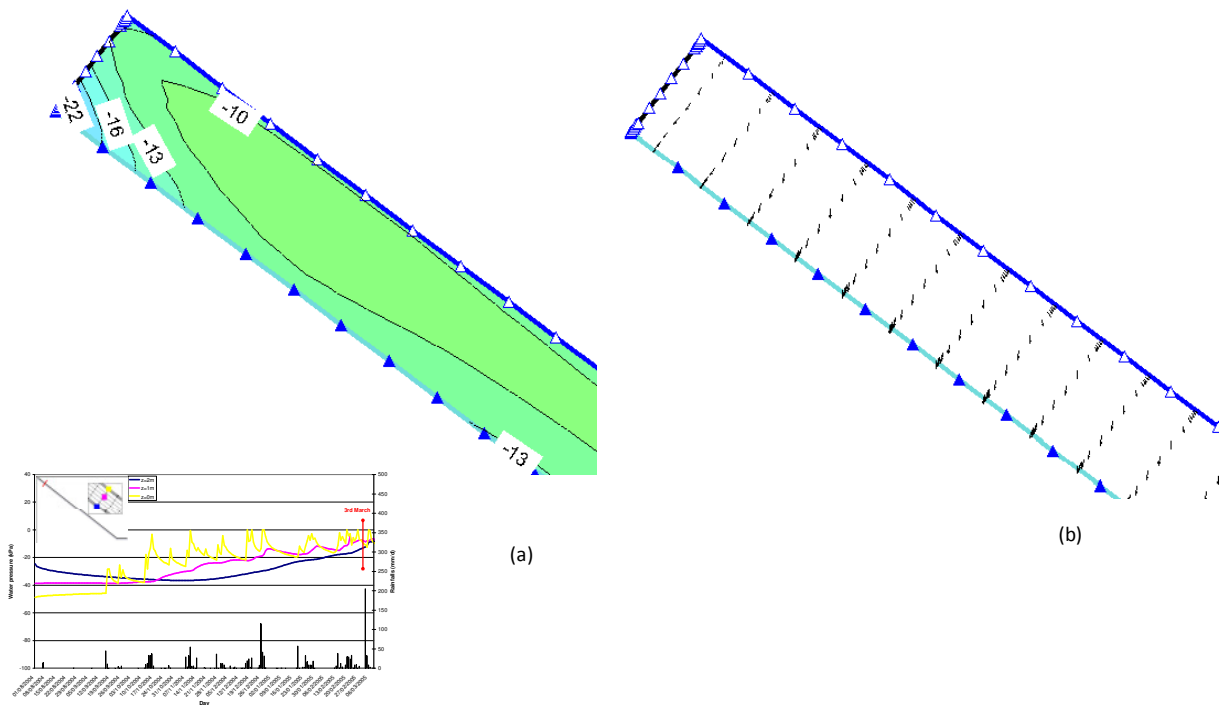


Figure 9. Pore pressure contours (a) and flow rate vectors (b) predicted on March 3 within the upper zone of the geometrical scheme, by assuming unit gradient at the base of the scheme and seepage flow at lateral boundaries

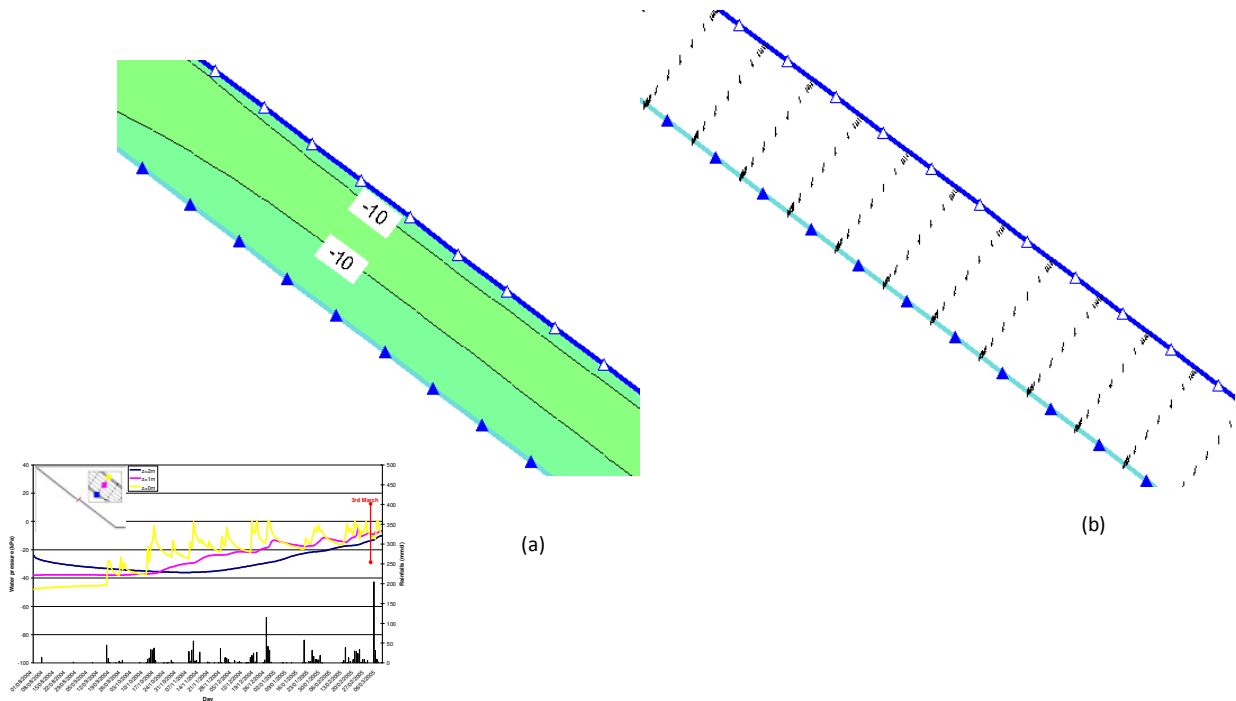


Figure 10. Pore pressure contours (a) and flow rate vectors (b) predicted on March 3 within the central zone of the geometrical scheme, by assuming unit gradient at the base of the scheme and seepage flow at lateral boundaries

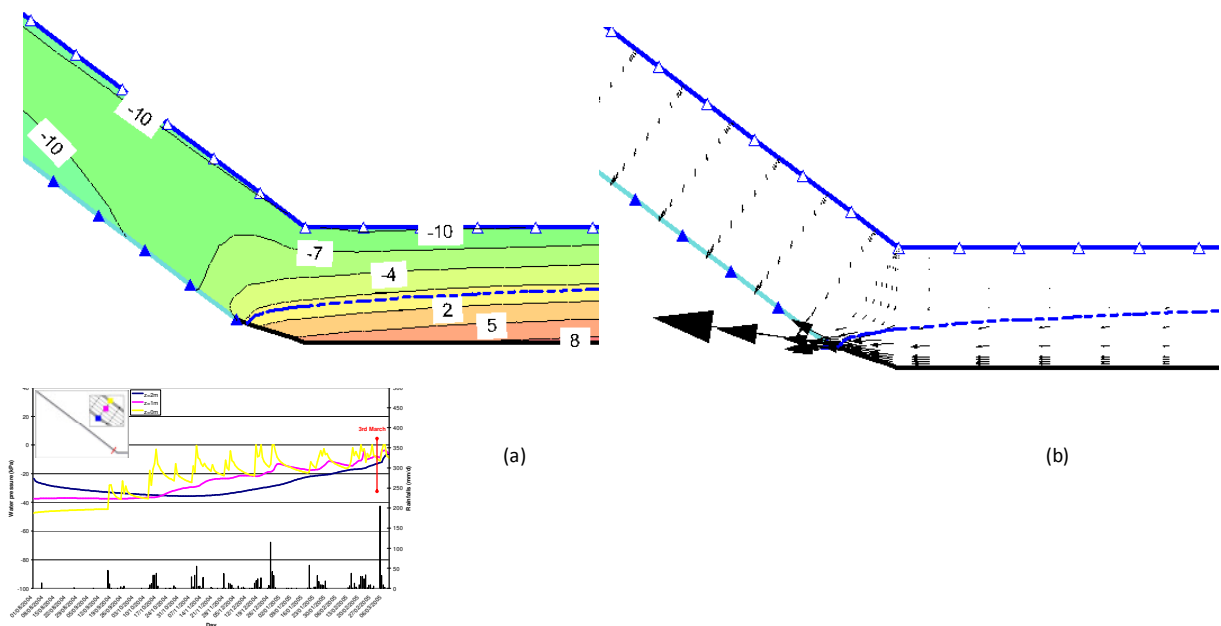




Figure 11. Pore pressure contours (a) and flow rate vectors (b) predicted on March 3 within the central zone of the geometrical scheme, by assuming unit gradient at the base of the scheme and seepage flow at lateral boundaries

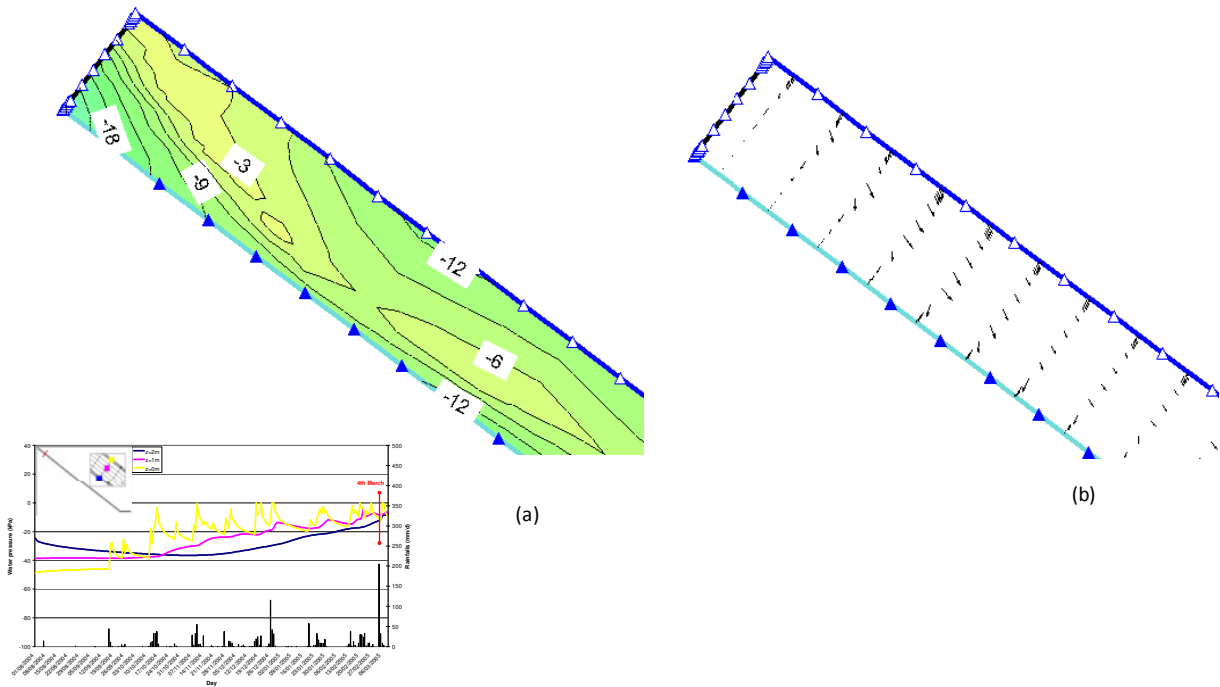


Figure 12. Pore pressure contours (a) and flow rate vectors (b) predicted on March 4 within the upper zone of the geometrical scheme, by assuming unit gradient at the base of the scheme and seepage flow at lateral boundaries

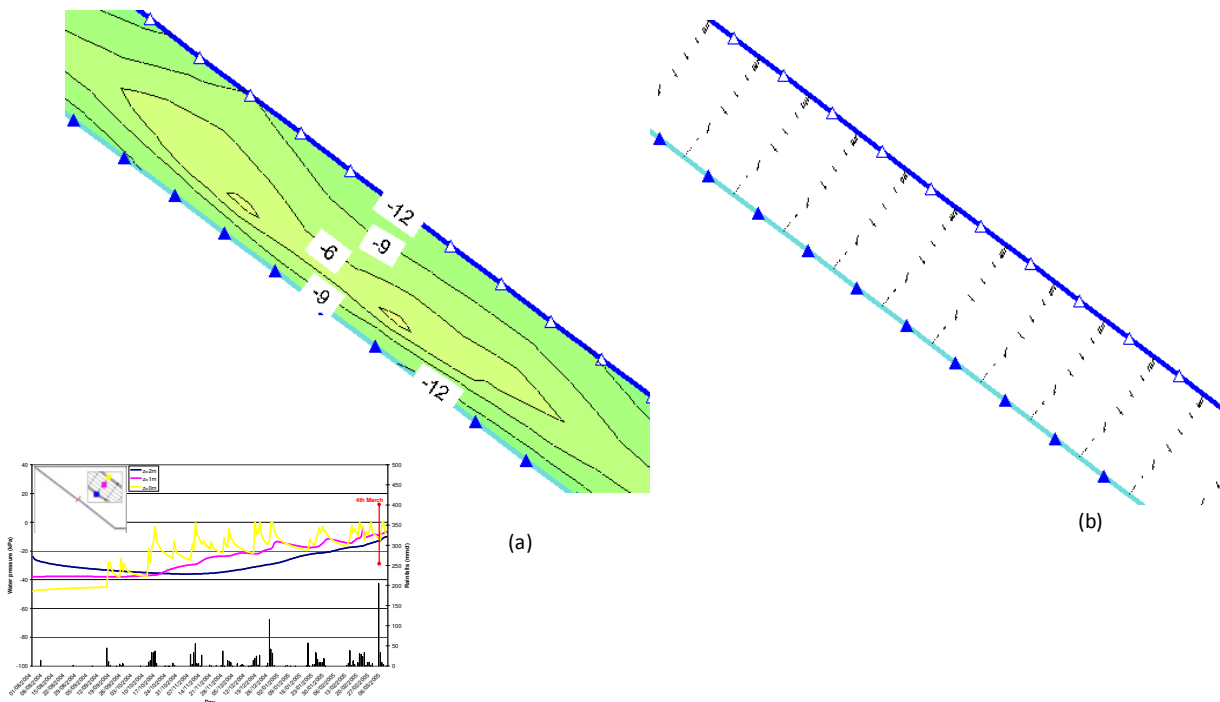


Figure 13. Pore pressure contours (a) and flow rate vectors (b) predicted on March 4 within the central zone of the geometrical scheme, by assuming unit gradient at the base of the scheme and seepage flow at lateral boundaries

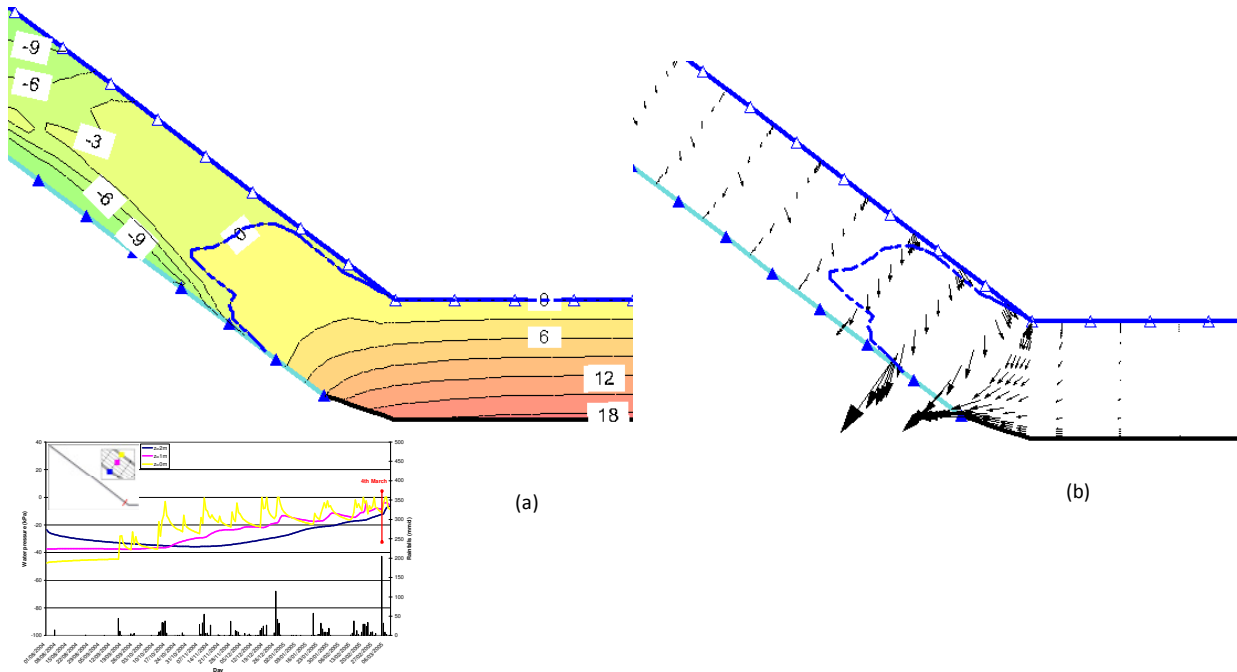


Figure 14. Pore pressure contours (a) and flow rate vectors (b) predicted on March 4 within the lower zone of the geometrical scheme, by assuming unit gradient at the base of the scheme and seepage flow at lateral boundaries

2.4 Pore water pressures and flow rates in the hypothesis of impervious slope bottom

In the assumption of impervious lowermost boundary (figures from 15 to 26) the only chance for the rain water seeping into the slope to come out is to flow through the downstream vertical surface as soon as pore water pressures is zero. This makes the hydraulic behavior of the system substantially different from that previously considered (free draining at the slope bottom).

However, during a long time period approaching to the dry season (Figure 15-17) the behavior under the two different hypotheses about the hydraulic boundary conditions provide similar results. This occurs while the seeping water has not yet reached the bottom surface, making the concerned hydraulic condition unable to influence numerical results.

Only subsequently, when the seeping water reaches the bottom surface, flow rate vectors become parallel to the slope (Figures 18-26). Vectors turn through downstream more or less at the time when pore water pressure exceed the atmospheric value.

In this case also, as for the previous one, the pore pressure contours indicate an extensive and progressive increase in pore water pressure (i.e., a decrease in suction) over time and a tendency for the geometrical domain to increase its water content. The

main difference with respect to the previous case is that pore water pressures become positive in middle and lower part of the geometrical domain during the wet period.

In the uppermost part (see Figures 15-18-21-24) the range of pore water pressures on 2004, 1st December is in between (-30) –(-12) kPa (slightly higher than value obtained in the free draining hypothesis); these values decrease down to (-17)-(-2)kPa on 2005, 1st February, then to (-9)-(0)kPa the day before the landslide trigger (2005, 3st February) and to (-12-3)kPa at onset of rupture.

In the middle part (Figures 16-19-22-25) and in the lowermost part of the slope (Figures 17-20-23-26) on same dates as above pore water pressures increase up to positive values with a maximum of 12 kPa in the middle part and of 18 kPa in the lowermost part on the day of the landslide.

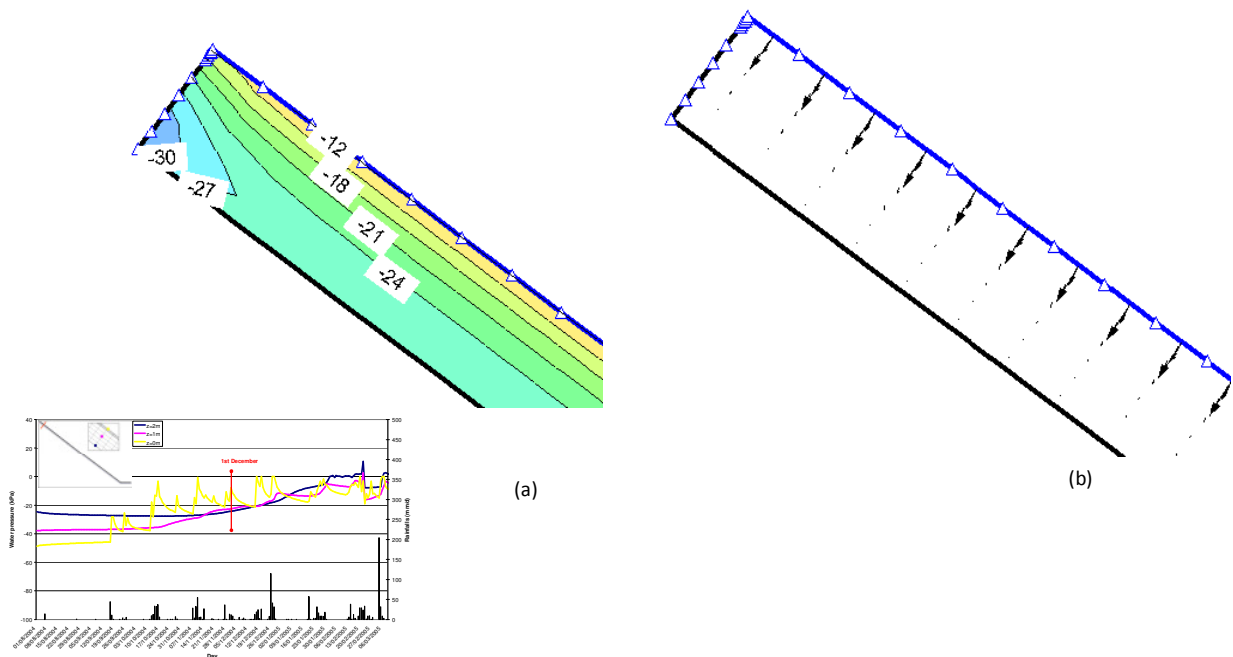


Figure 15. Pore pressure contours (a) and flow rate vectors (b) predicted on December 1 within the upper zone of the geometrical scheme, by assuming impervious base of the scheme and seepage flow at lateral boundaries

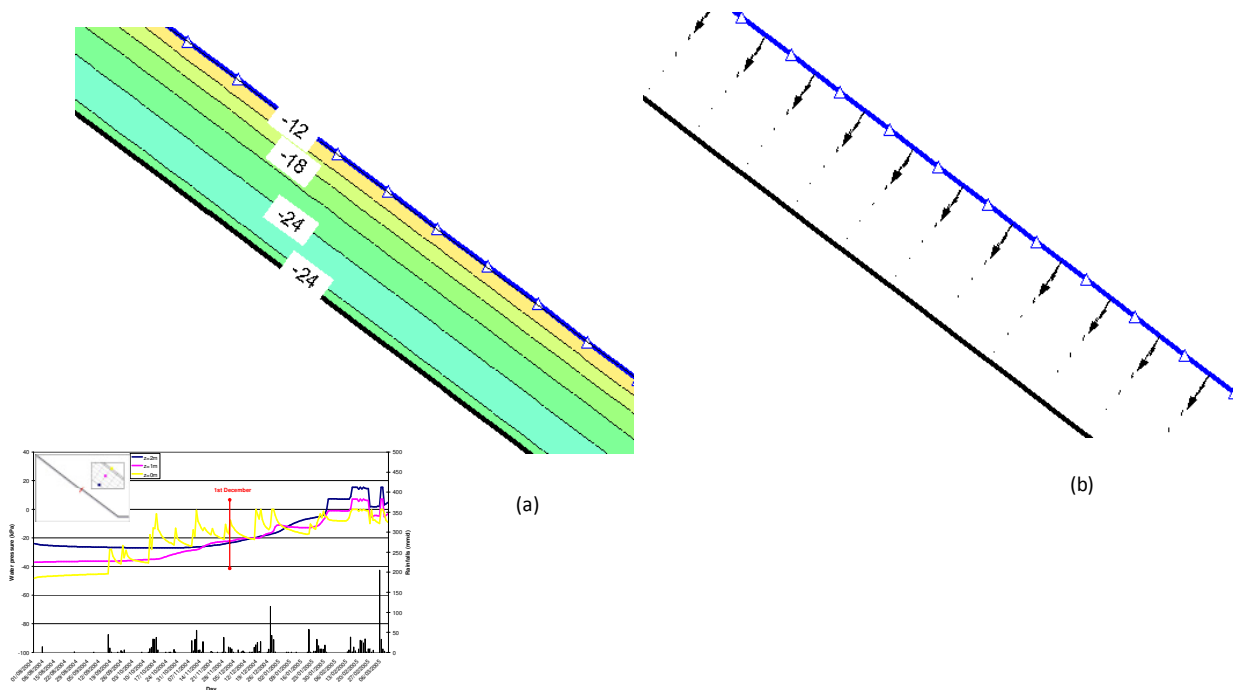


Figure 16. Pore pressure contours (a) and flow rate vectors (b) predicted on December 1 within the central zone of the geometrical scheme, by assuming impervious base of the scheme and seepage flow at lateral boundaries

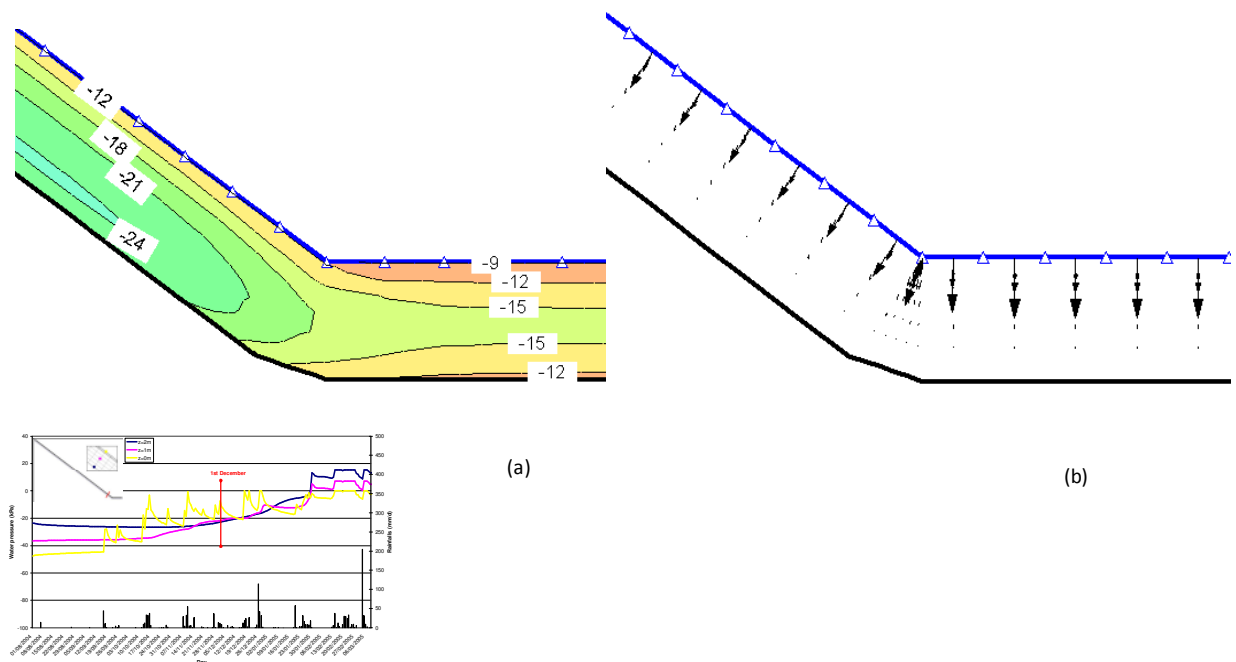


Figure 17. Pore pressure contours (a) and flow rate vectors (b) predicted on December 1 within the lower zone of the geometrical scheme, by assuming impervious base of the scheme and seepage flow at lateral boundaries

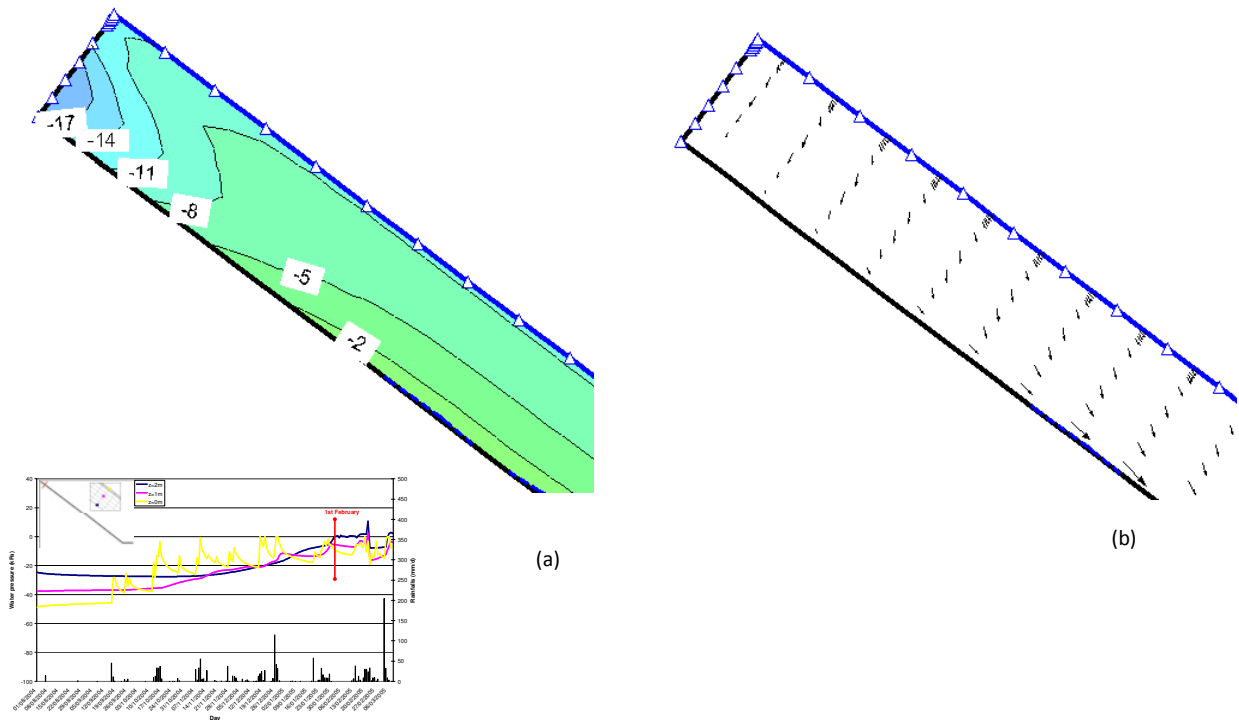


Figure 18. Pore pressure contours (a) and flow rate vectors (b) predicted on February 1 within the upper zone of the geometrical scheme, by assuming impervious base of the scheme and seepage flow at lateral boundaries

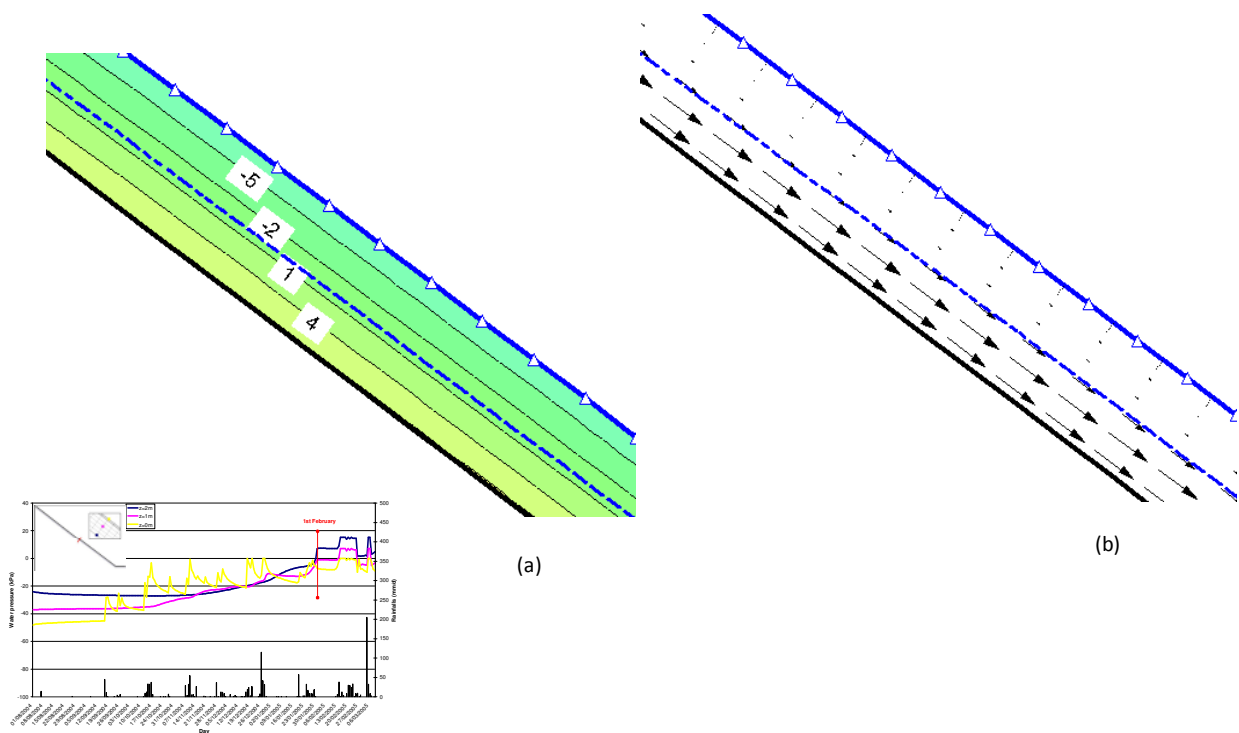


Figure 19. Pore pressure contours (a) and flow rate vectors (b) predicted on February 1 within the central zone of the geometrical scheme, by assuming impervious base of the scheme and seepage flow at lateral boundaries

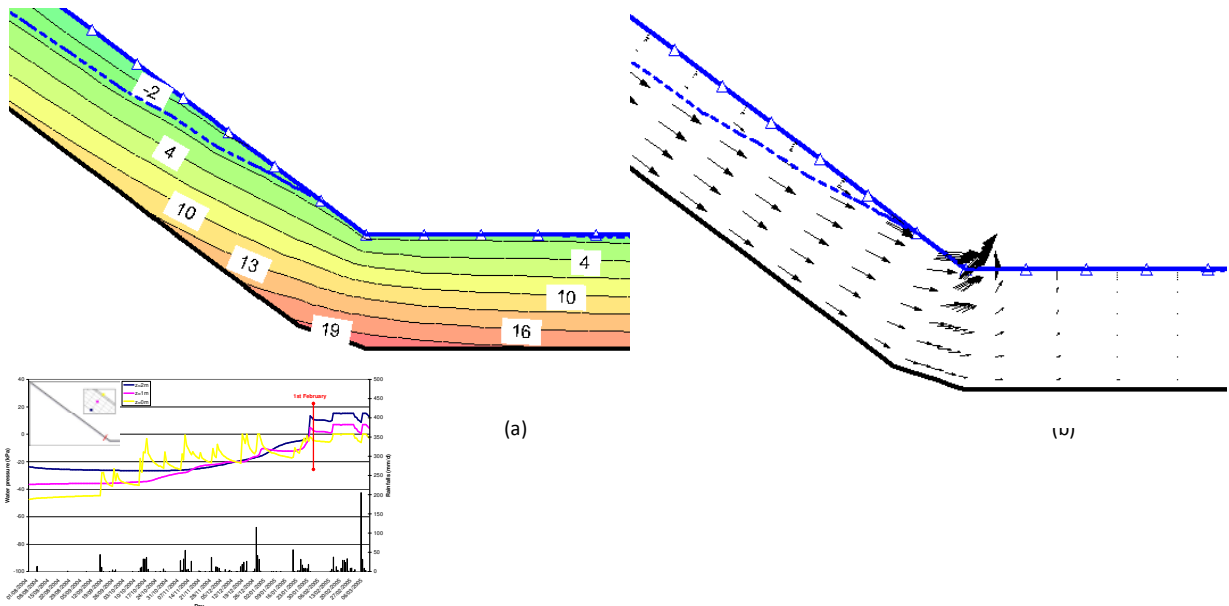


Figure 20. Pore pressure contours (a) and flow rate vectors (b) predicted on February 1 within the lower zone of the geometrical scheme, by assuming impervious base of the scheme and seepage flow at lateral boundaries

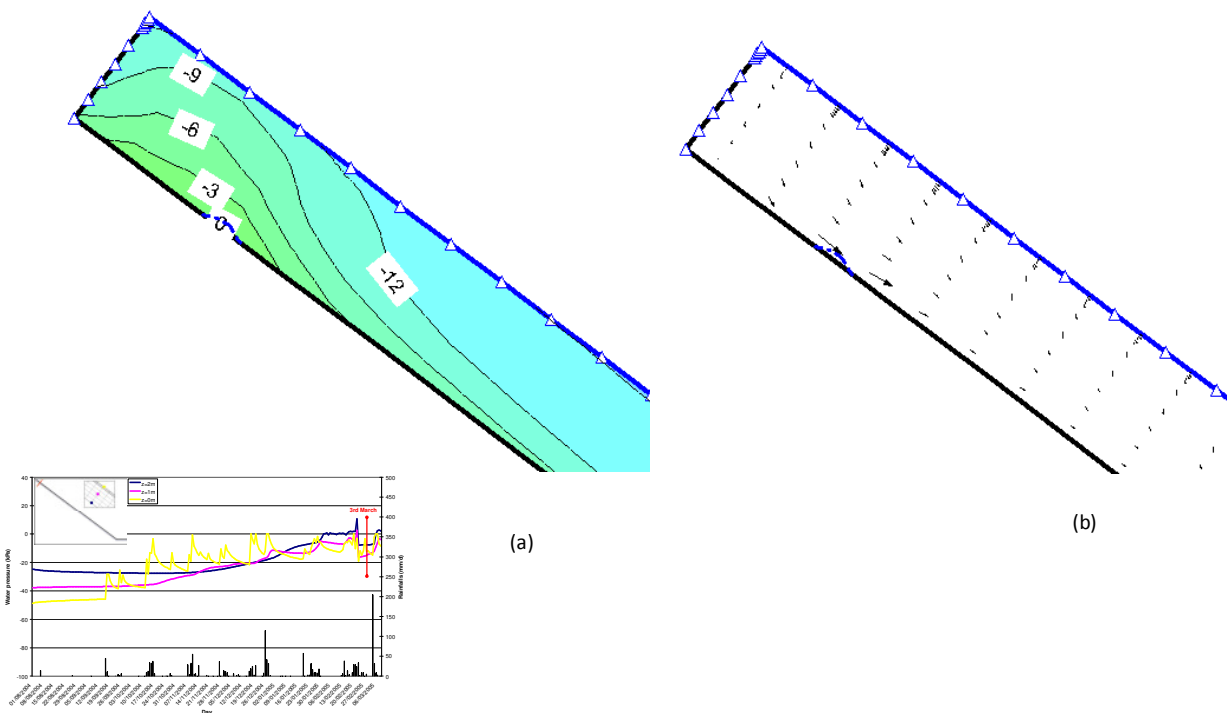


Figure 21. Pore pressure contours (a) and flow rate vectors (b) predicted on March 3 within the upper zone of the geometrical scheme, by assuming impervious base of the scheme and seepage flow at lateral boundaries

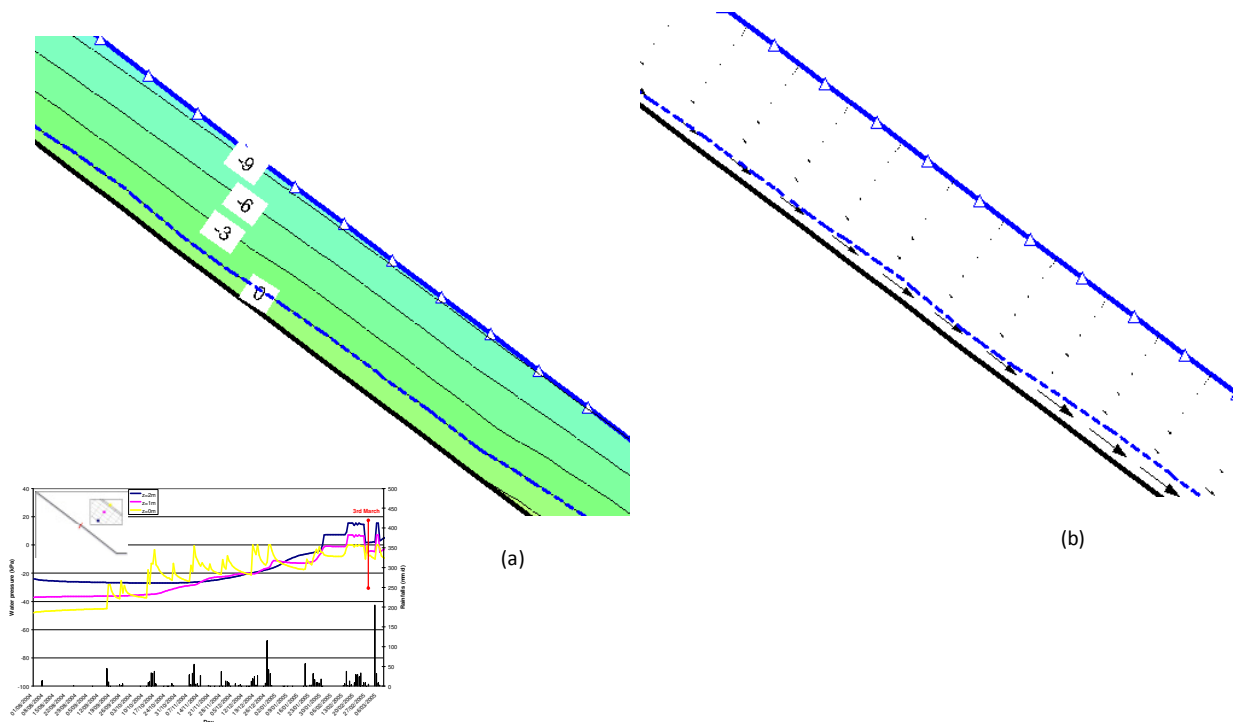


Figure 22. Pore pressure contours (a) and flow rate vectors (b) predicted on March 3 within the central zone of the geometrical scheme, by assuming impervious base of the scheme and seepage flow at lateral boundaries

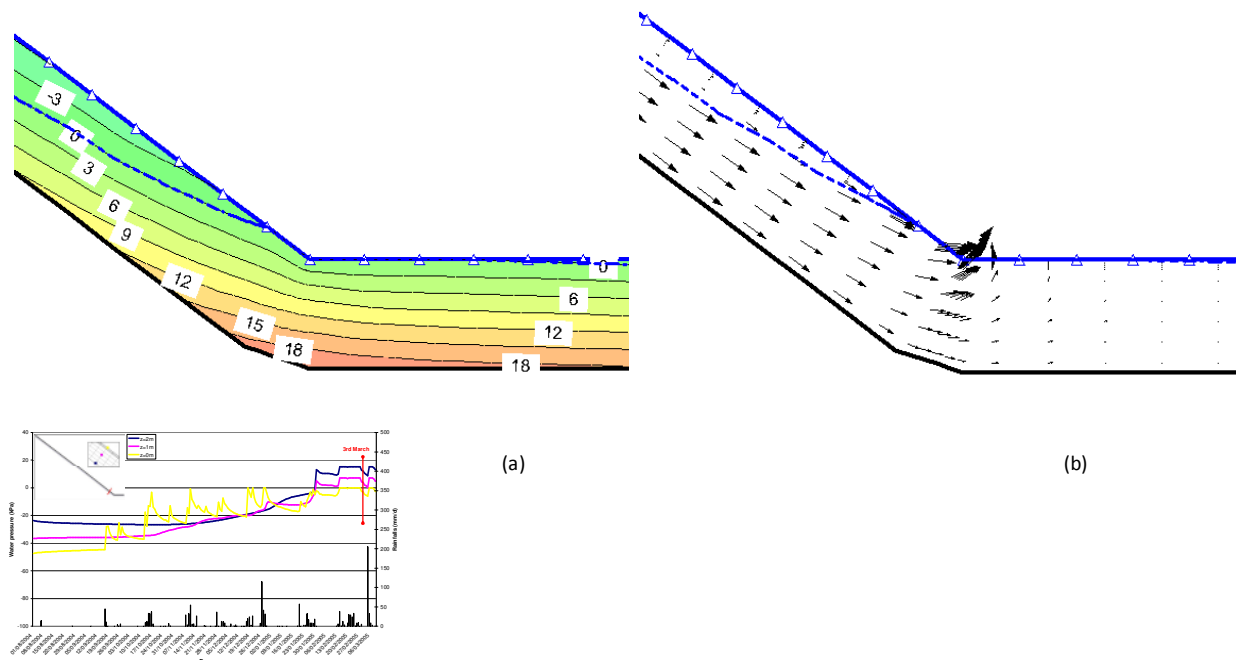


Figure 23. Pore pressure contours (a) and flow rate vectors (b) predicted on March 3 within the lower zone of the geometrical scheme, by assuming impervious base of the scheme and seepage flow at lateral boundaries

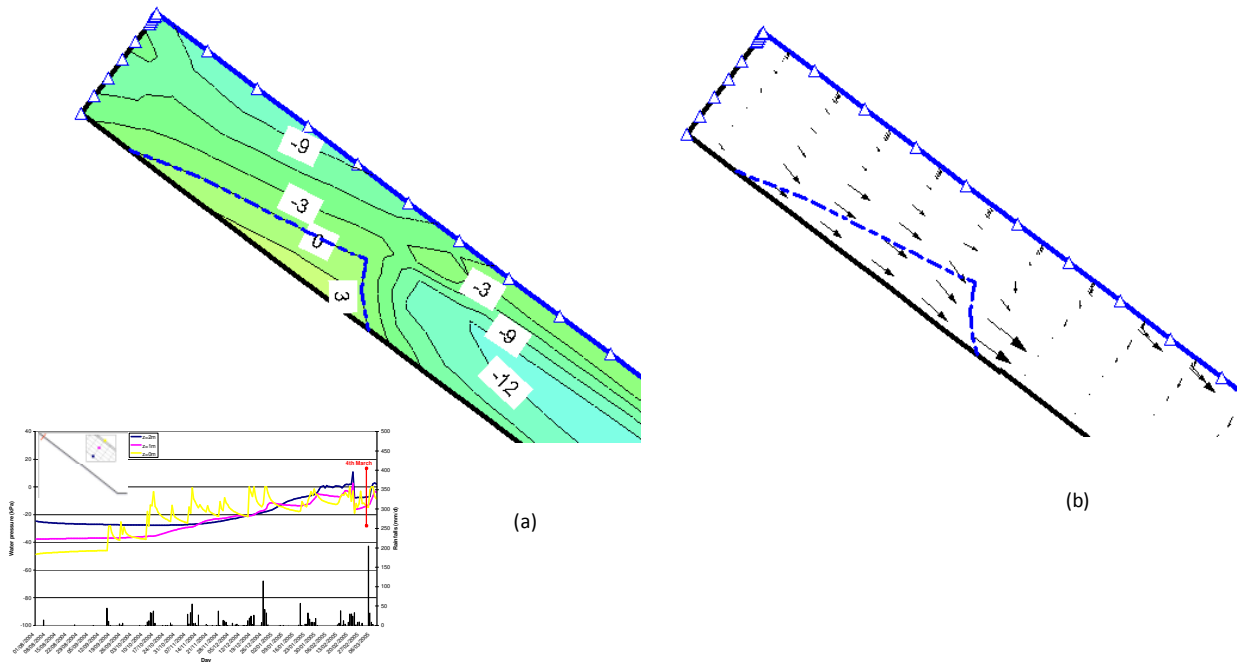


Figure 24. Pore pressure contours (a) and flow rate vectors (b) predicted on March 4 within the upper zone of the geometrical scheme, by assuming impervious base of the scheme and seepage flow at lateral boundaries

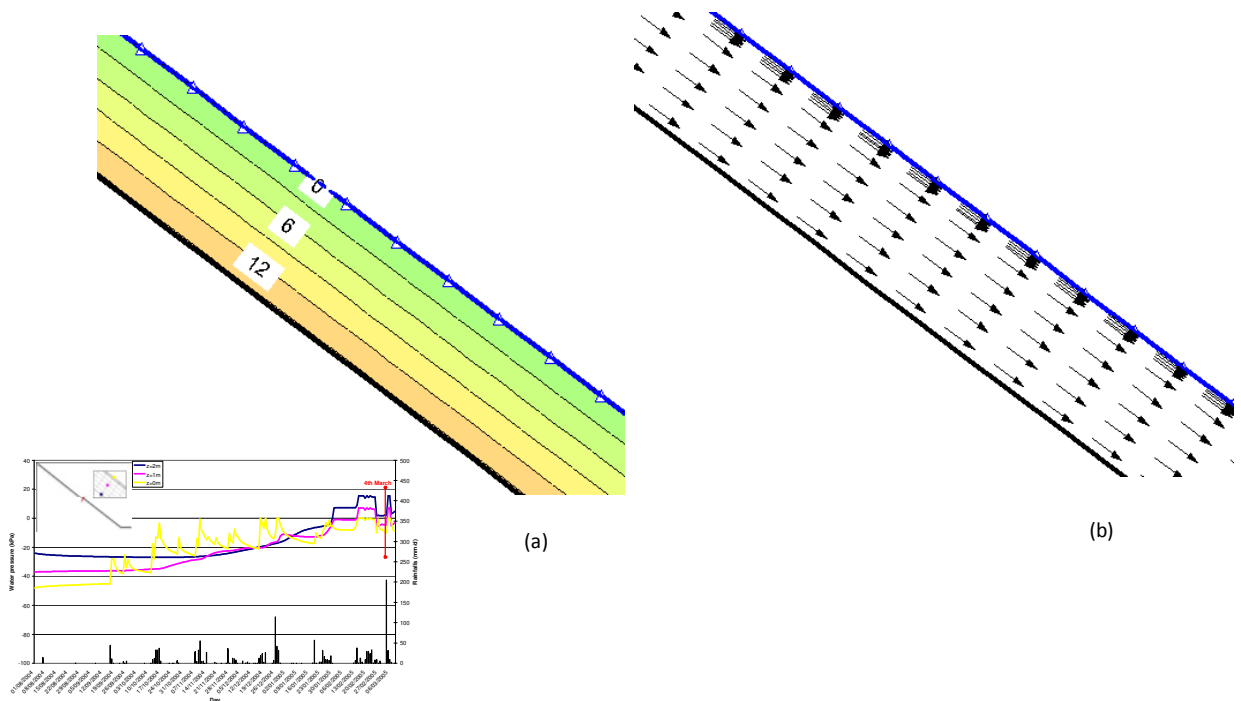


Figure 25. Pore pressure contours (a) and flow rate vectors (b) predicted on March 4 within the central zone of the geometrical scheme, by assuming impervious base of the scheme and seepage flow at lateral boundaries

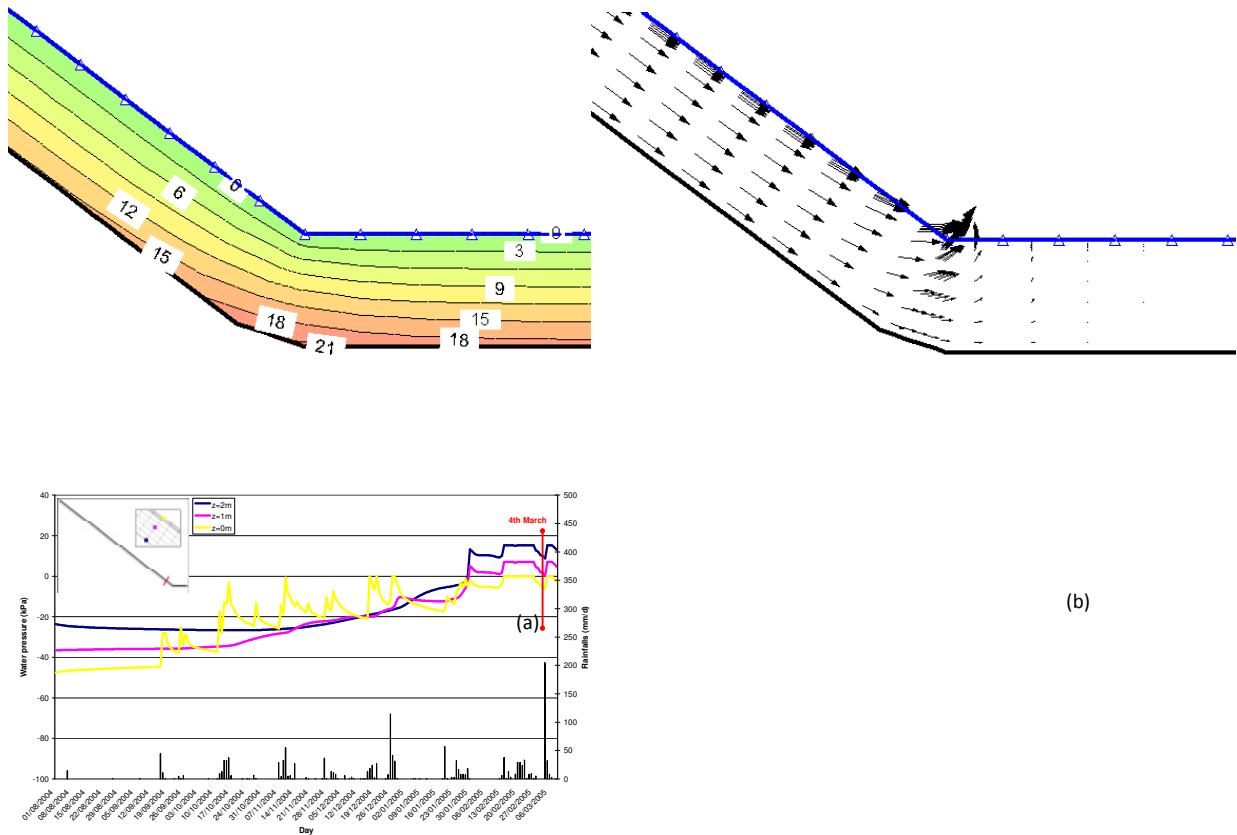


Figure 26. Pore pressure contours (a) and flow rate vectors (b) predicted on March 4 within the central zone of the geometrical scheme, by assuming impervious base of the scheme and seepage flow at lateral boundaries

2.5 Safety factors

The global safety factor has been computed by assuming a unique potential slip surface at the bottom of the pyroclastic cover coming out in the upstream and downstream part of the slope.

Soil parameters assumed are consistent with those illustrated in a previous report for the pyroclastic soils involved in the landslide ($c'=0$; $\phi'=37^\circ$; $\gamma_{\text{sat}}=1.8 \text{ t/m}^3$).

Safety factors development over time in the free draining hypothesis at the bottom surface have been computed and represented for different values of the friction angle associated to soil suction (Figure 27). The different positioning of each curve show clearly what effects the suction level exerts on slope safety conditions. Each curve indicates that the safety factor is more or less constant up to the landslide date, when it decreases abruptly towards unity. In the free draining hypothesis the analysis is quite capable in the diagnosis of the instability phenomenon by indicating lowest safety factor the landslide time.

Global safety factor values (along the entire potential slip surface) over time in the bottom impervious hypothesis have been obtained by assuming two different values for the friction angle associated to the suction. In this case more significant build up of



pore water pressure during a rain event and subsequent dissipation phenomena make the trend of the safety factor more articulated than in the other case analyzed. Also in this case an abrupt decrease of safety factor occurs at the landslide time but the value does not represent in absolute the minimum one.

The conclusion about which one between the two lowermost boundary conditions investigated was that likely to have taken place in the reality may be drawn on the basis of which of them was able in interpreting the occurrence of the flowslide on March, 4. The results in terms of global safety factors indicate clearly that the lowermost boundary condition of unit gradient was able in depicting a scenarious with a landslide only at the triggering time, while that of impervious lowermost boundary condition was not. As matter of facts, the former condition provides the minimum (and close to unity) value of the safety factor development over time at the triggering time, while the latter indicates systematically safety factor values less than unity already before the triggering time. Such values are also less than the one associated with the triggering time itself, which clearly does not interpret the occurrence of the flowslide.

3. Rain induced effects for rain forecasts

As shown above the interpretation of the flowslide occurred in Nocera on March, 4 is well supported by the knowledge of the rain history occurred near the landslide site over the entire season preceding the event. In the previous sections this rain history has been turned into a development of soil suctions and safety factors over time through a mathematical-numerical model reproducing the rain infiltration in isothermal and plane strain conditions.

For the fourteen hours preceding the triggering time a weather prediction has been made available by the CIRA institution by using the COSMO LM code set at the 2.8 Km configuration. This prediction is twofold, since it provides both a maximum and medium value of the expected rain height over the just mentioned time length.

As obvious, some discrepancies between predicted and measured rains arises. The maximum forecasted rains (139 mm) are very close to the observed ones (147 mm). The medium forecasted rains (81 mm) are instead significantly less than the observations.

The entity of these discrepancies, above implicitly judged by merely looking at the error percentages between measurements and observation, may be evaluated in a different light, looking at the differences the discrepancies in rains determine in terms of quantities closely faced with the slope safety conditions, i.e. soil suction and safety factor values.

In this section the discrepancies between forecasted and measured rains are hence judged after have turned them in soil suction and safety factor differences.

Two additional analyses have been carried out by using the forecasted rains. They were both carried out by assuming a lowermost boundary condition of unit gradient since previously it resulted the most reliable between the two ones that may be hypothesized. In both analyses the real rains have been adoptes as uppermost boundary conditions until fourteen hours before the triggering time. For the last fourteen hours the maximum forecasted rains were assumed in one analysis, while the medium forecasted rains were assumed in the other.



Worth noting is that the procedure of merging in the analysis real rains with forecasted rains does make sense in the philosophy of an early warning system development. As a matter of fact, it would be advisable that an early warning system be based on computing the start conditions (in terms of soil suction and safety factor) by referring to the past actual rains, before computing the future response on the basis of forecasted rains.

Results obtained from the analyses of forecasted rains are compared with results obtained from those analyses of the real rains already described previously.

Figures from 29 to 34 show results in terms of suction over time while figures 35 and 36 plot development of safety factors over time. It is possible to observe that neither the maximum (Figures 29, 31, 33, 35) nor the medium (Figures 30, 32, 34, 36) determine effects appreciably different from those coming from actual rains.

This is essentially due to the fact that the differences in rains take place in a state of the system which facilitate the run off. The starting point of the medium, i.e. that fourteen hours before the triggering time, is in fact that of a nearly saturated state, so that the capability the system has in adsorbing water is reduced to a threshold near that associated with the rain intensities of the medium forecast. This involves that the higher intensities of the maximum forecast and actual rains might only be introduced within the system by forcing at the uppermost boundary pore water pressures exceeding the atmospheric value, that is physically inconsistent.

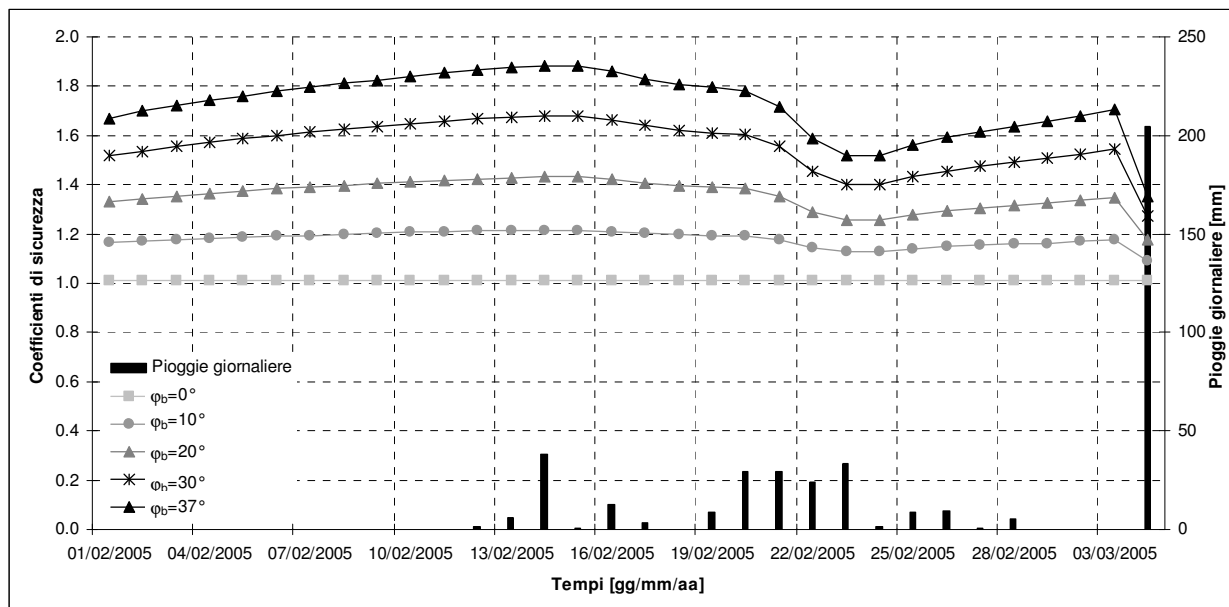


Figure 27. Global safety factor of the slope in the free draining hypothesis at the bottom

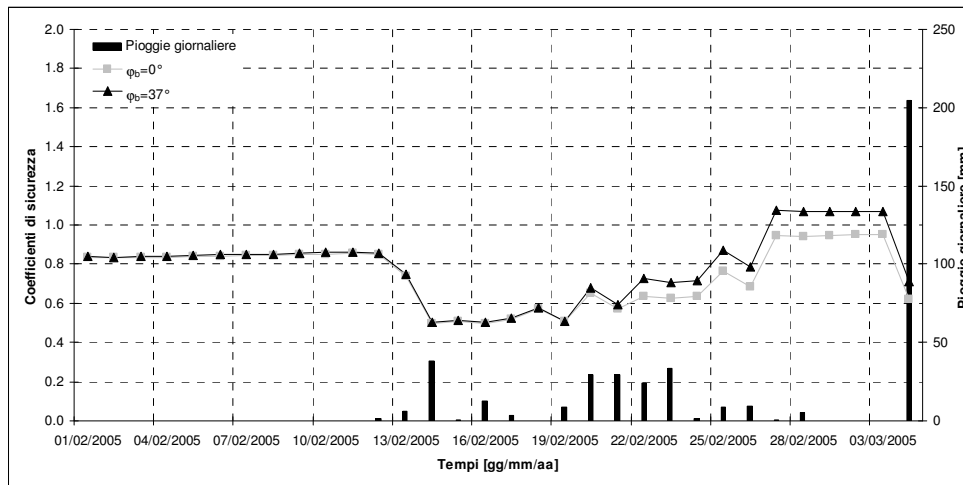


Figure 28. Global safety factor of the slope in the free draining hypothesis at the bottom

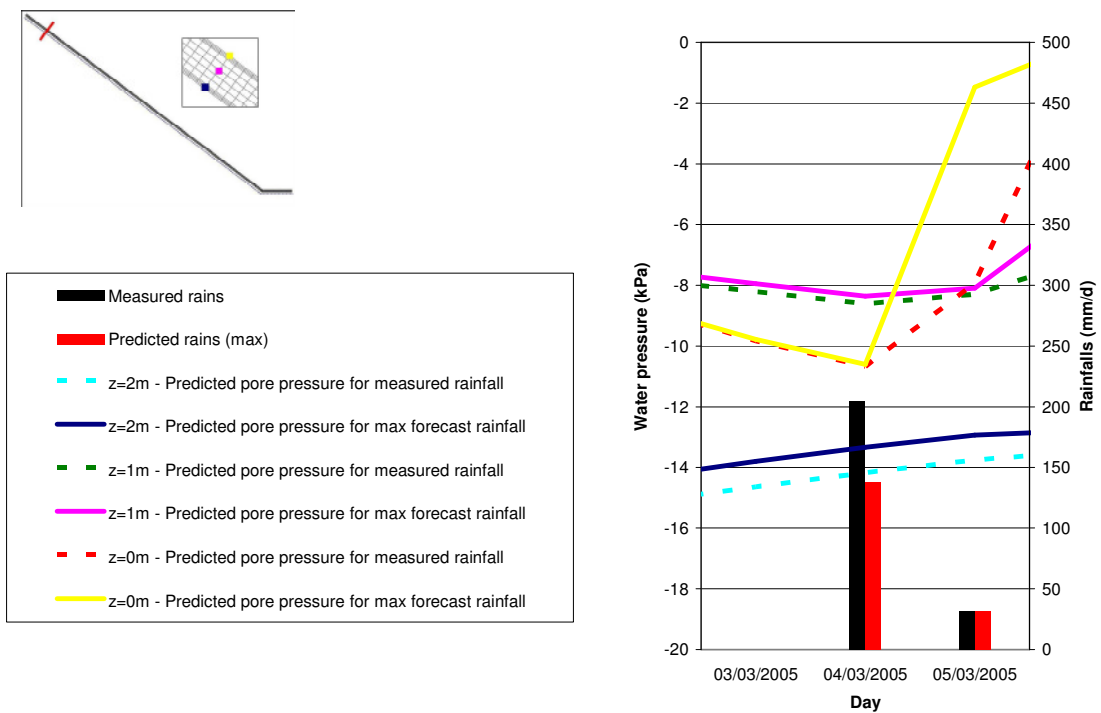


Figure 29. Development of suction over time due to predicted maximum rains in the uppermost part of the slope

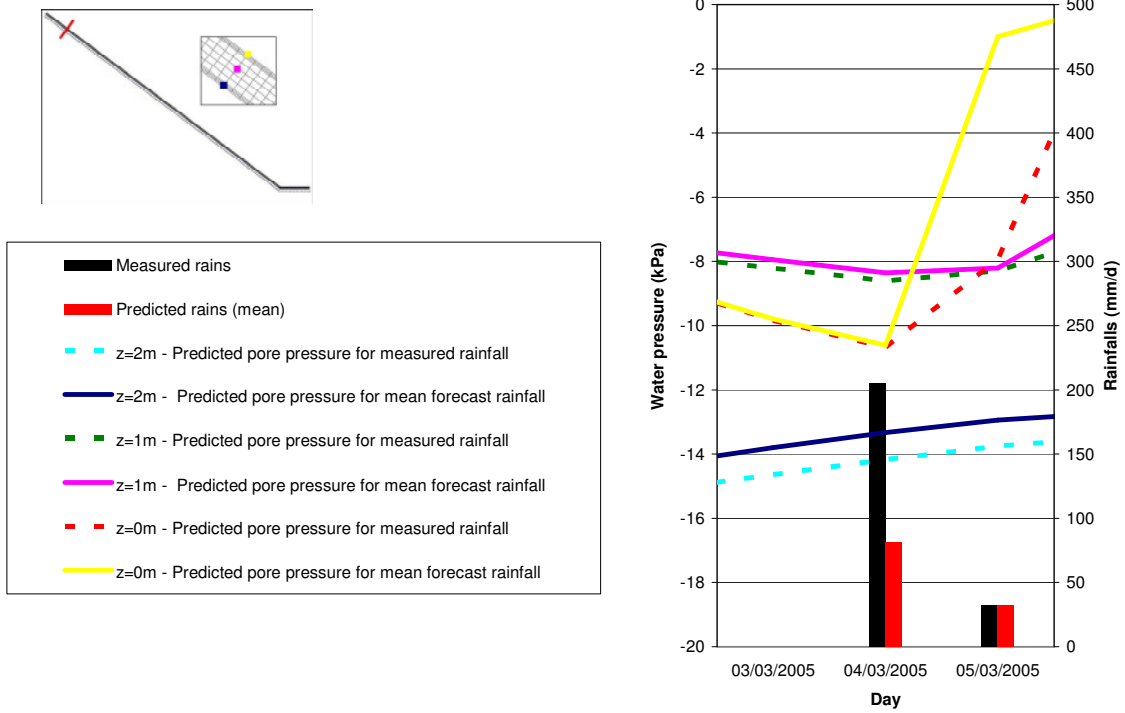


Figure 30. Development of suction over time due to predicted mean rains in the uppermost part of the slope

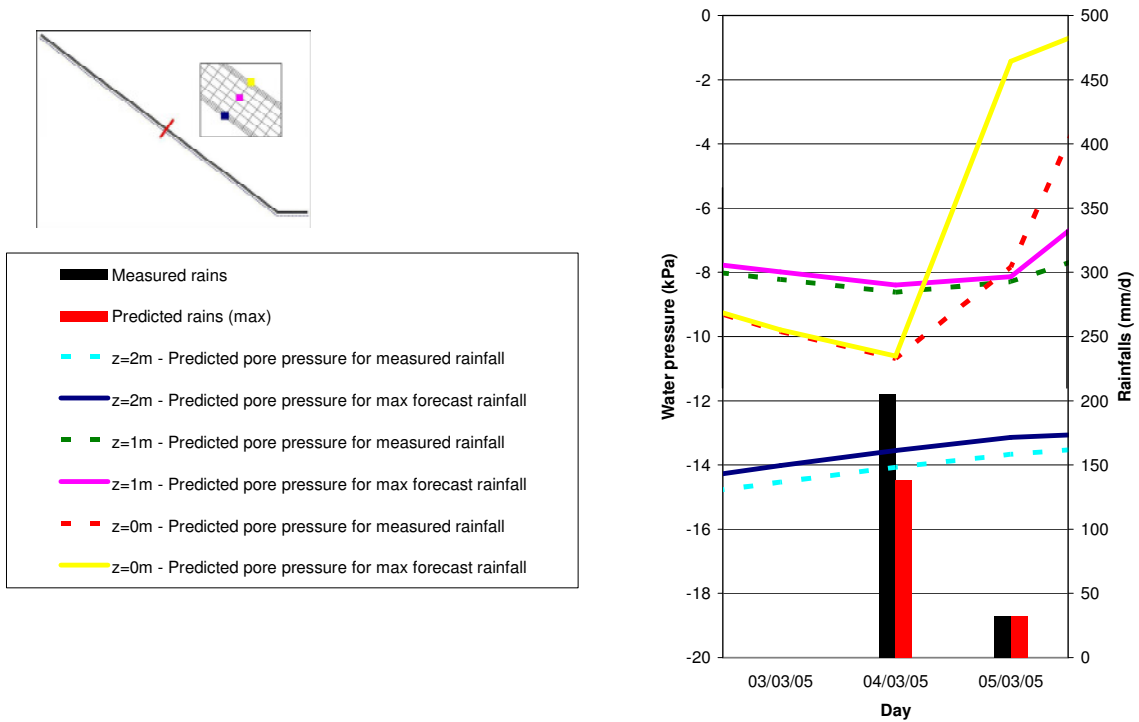


Figure 31. Development of suction over time due to predicted maximum rains in the medium part of the slope

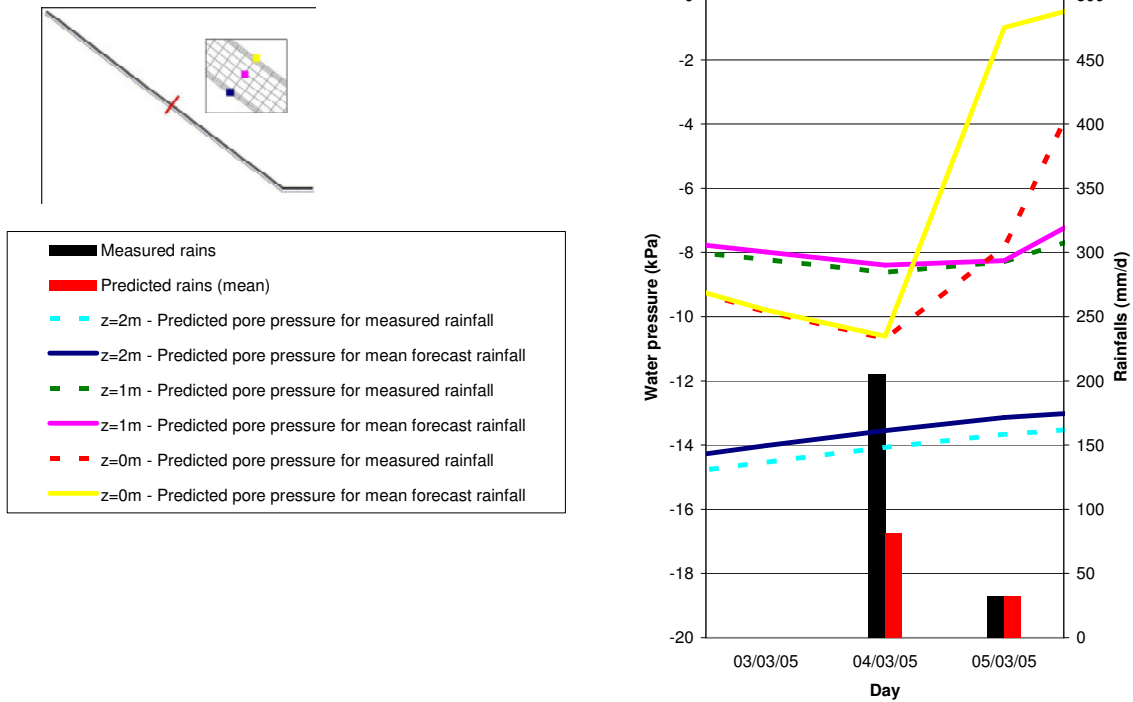


Figure 32. Development of suction over time due to predicted maximum rains in the medium part of the slope

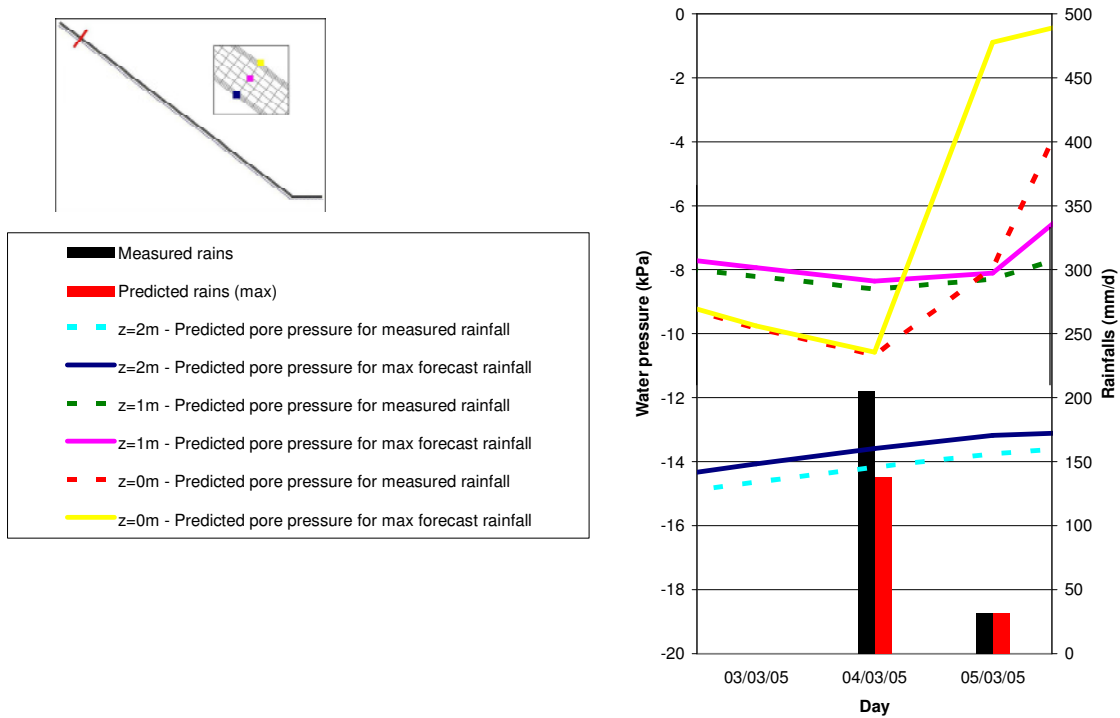


Figure 33. Development of suction over time due to predicted maximum rains in the medium part of the slope

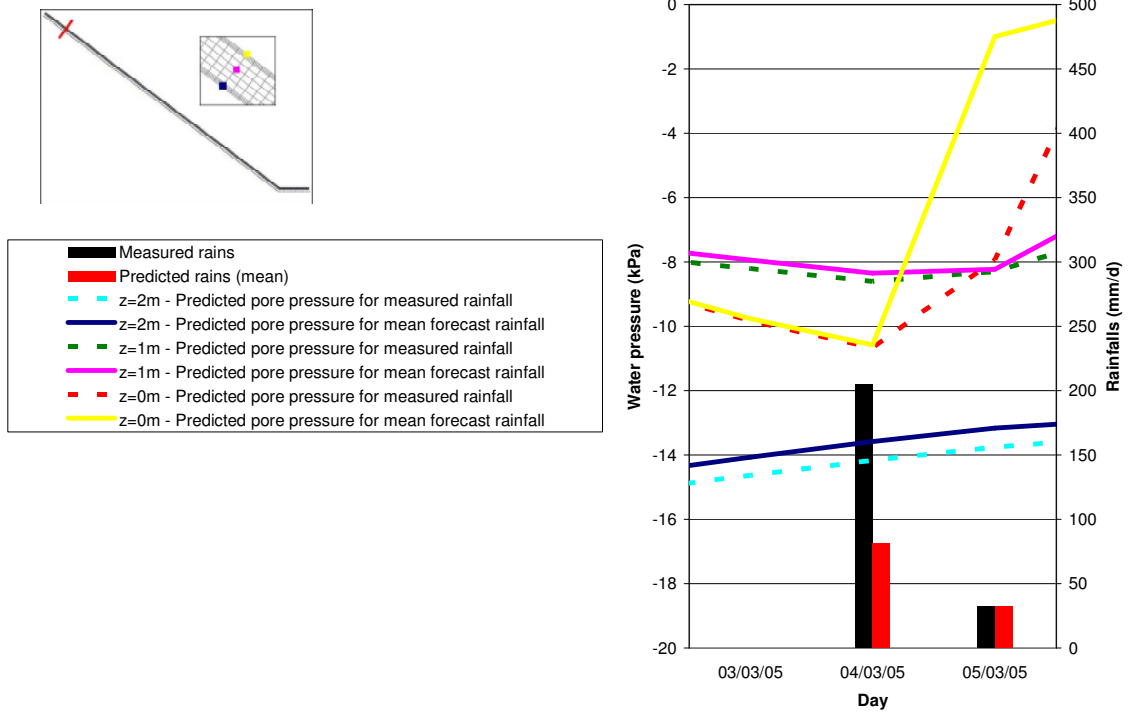


Figure 34. Development of suction over time due to predicted mean rains in the lowermost part of the slope

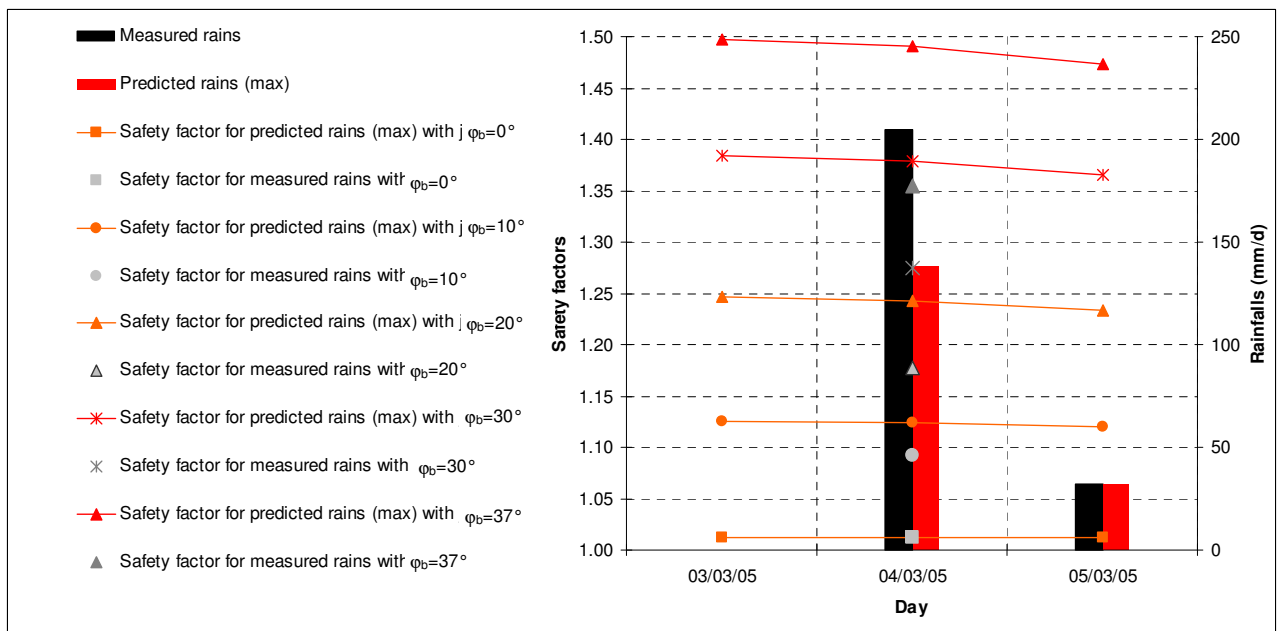


Figure 35. Global safety factor of the slope in the free draining hypothesis at the bottom, for the predicted maximum rains

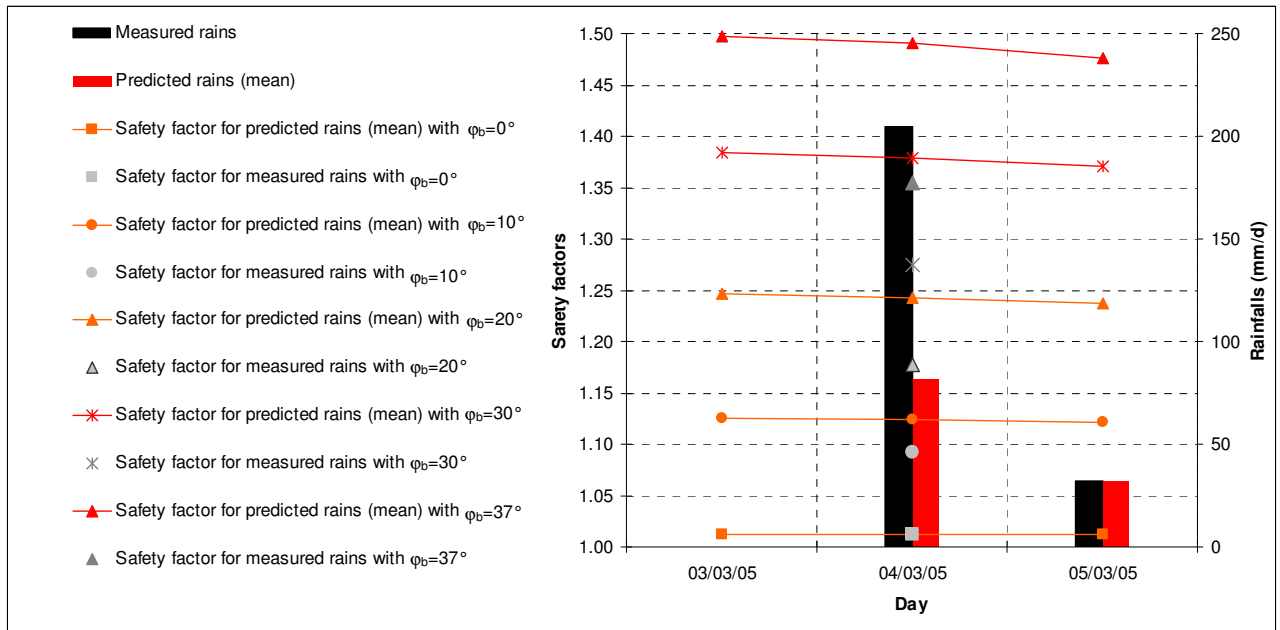


Figure 36. Global safety factor of the slope in the free draining hypothesis at the bottom, for the predicted medium rains